Noninvasive Cardiac Electrical Imaging of Activation Sequence and Activation Recovery Interval, and Localization of Ventricular Arrhythmias

A DISSERTATION
SUBMITTED TO THE FACULTY OF
THE UNIVERSITY OF MINNESOTA
BY

Ting Yang

IN PARTIAL FULFILLMENT OF THE REQUIERMENTS
FOR THE DEGREE OF
DOCTOR OF PHILOSOPHY

Advisor: Bin He, Ph.D.

January 2018

Acknowledgements

I would like to express my most sincere appreciation to my advisor, Dr. Bin He, for his guidance and support over the past four years. He led me to this research and gave me numerous advices throughout the program. I also want to thank my dissertation committee, Dr. Lin Yee Chen, Dr. Alexander Opitz and Dr. Zhi Yang, for their time and valuable comments.

I would like to thank Dr. Steven M. Pogwizd and Dr. Gregory P. Walcott, professors from University of Alabama at Birmingham for their collaboration, technical support and useful discussion. Thanks to Mr. Qi Jin and Mr. Liqun Wu, doctors from Shanghai Ruijin Hospital, for collaboration and providing clinical data.

I am honored to work with many lab colleagues who have been in the Biomedical Functional Imaging and Neuroengineering Laboratory at University of Minnesota. Special thanks to Dr. Long Yu and Dr. Zhaoye Zhou for their help in the project, and in animal and human experiments. They taught me a lot and helped me getting started. They are also great team members to work with. I also want to thank Dr. Huishi Zhang, Mr. Abbas Sohrabpour and Mr. Daniel Suma for useful technical discussions.

In addition, I am grateful to all the other lab members whom I have worked with: Dr. Yunfeng Lu, Dr. Nessa Johnson, Dr. Abhrajeet Roy, Dr. Jiaen Liu, Dr. Leo Mariappan, Dr. Xiaotong Zhang, Ms. Kaitlin Cassady, Dr. Haiteng Jiang, Dr. Jianjun Meng, Dr. Qi Shao, Dr. Yanbin Xu, Mr. Zhengxiang Cai, Ms. Michelle Case, Mr. Chris Cline, Mr. Christopher Coogan, Mr. Brad Edelman, Mr. Amir-Hossein Hosseini, Ms. Rachel Niu, Mr. Sina Shirinpour, Mr. James Stieger, Mr. Vishal Vijayakumar, Mr. Yicun Wang, Ms. Shuai Ye and Mr. Kai Yu. It's their professional attitude towards work and insights that keeps me moving forward.

Dedication

This dissertation is dedicated to my parents, Mr. Sendong Yang and Mrs. Cairong Cui, for bringing me up, for loving me unconditionally, and for supporting me through the hard days. This dissertation is also dedicated to my dear friends. Without them, I would not become who I am.

Abstract

This dissertation research aims to develop and evaluate methods for noninvasive cardiac imaging of activation sequence and activation recovery interval (ARI), and localization of ventricular arrhythmias. It includes (1) developing a novel imaging method (SSF, Spatial gradient Sparse in Frequency domain) for the reconstruction of activation sequences in ventricular arrhythmias, (2) developing ARI imaging technique to reconstruct the ARI maps in premature ventricular contraction (PVC) patients from body surface potential maps, (3) proposing a CNN-based (convolutional-neural-network-based) method to localize origins of PVCs from 12-lead electrocardiography (ECG).

SSF is implemented in the frequency domain, and the activation time was encoded in the phase information of the solution. The performance of SSF was evaluated in computer simulation and a swine model with myocardial infarction. SSF is the first noninvasive imaging method reported that could reconstruct the reentry circuit in 3-dimensional space. SSF achieved better performance with less computational time.

ARI imaging reconstructed 3D ARI maps in ventricles, which were compared with the endocardial ARI maps from CARTO recordings. From the analysis of 100 PVC beats in ten patients, the results suggest that it could serve as an alternative of evaluating global dispersion of ventricular repolarization and could guide ablation procedure in PVC patients.

The CNN-based method consists of two CNNs (Segment CNN and Epi-Endo CNN). The inputs are from 12-lead ECG. The origins of PVC are localized by calculating the weighted center of gravity of classification returned by the CNNs. It was evaluated in computer simulation and in 90 PVC beats from nine patients. The results demonstrate the capability and merits of the proposed method for localization of PVC. This work suggests a new approach for cardiac source localization of origins of arrhythmias using only the 12-lead ECG by means of CNN.

Table of Contents

List of Tables

List of Figures

Chapter 1

Introduction

1.1 Overview

Sudden cardiac death (SCD) is a leading cause of death worldwide. According to the 2013 statistics report from the American Heart Association, the incidence of out-of-hospital cardiac arrest is 359,400 cases with a survival rate of 9.5% and the incidence of in-hospital cardiac arrest is 209,000 cases with a survival rate of 23.9%. A majority of SCD cases are caused by ventricular arrhythmias and especially by ventricular fibrillation. To treat ventricular arrhythmias, catheter ablation procedures usually require extensive invasive electrophysiological mapping to determine the arrhythmogenic substrate, and thus put patients in the electrophysiology laboratory for prolonged periods. Therefore, cardiac electrical imaging technique is a promising approach in noninvasively reconstructing activation sequences or action potentials of the whole heart. By detecting the earliest activated location, it allows the physicians to know the potential area of ablation before inserting a catheter into the heart, which improves the effectiveness and efficiency of catheter ablation and reduces the overall procedure time. By reconstructing action potentials, it could identify regions with low potentials and estimate the extent of myocardial infarction. By reconstructing the activation sequences, it helps in understanding the mechanism of ventricular arrhythmias.

Dispersion of ventricular repolarization due to abnormal activation contributes to the susceptibility to cardiac arrhythmias. Studies have shown the relationship between inhomogeneity of ventricular repolarization and enhanced ventricular arrhythmia vulnerability. Activation recovery interval (ARI) has been used to understand the properties of ventricular repolarization. It has the advantage of being able to be extracted from multiple, simultaneously recorded electrograms and reflecting the dynamics and spatial characteristics of repolarization.

The 12-lead ECG has been widely used as a diagnostic test for cardiac arrhythmias since its invention. It is the most accessible noninvasive data and it can be recorded rapidly

with a portable equipment for a long time using a Holter monitor. Neural network is well known for recognizing patterns and classification. The accuracy can be higher than 90% given ample training samples. The combination of these two would have the advantage of data being easily collected, analysis quickly finished and relatively good accuracy obtained.

1.2 Motivation

Our group has conceptualized and pioneered a novel approach for a noninvasive 3-dimensional cardiac electrical imaging (3DCEI) technique. This physical-model-based approach images the cardiac electrical activities throughout the myocardium based on equivalent-current-density distributions without an electrophysiological assumption. Computer simulation and animal studies have demonstrated the capability of this approach for imaging activation sequences throughout the ventricular myocardium. However, a few questions remain to be answered: Can this method be applied to a reentrant ventricular tachycardia, whose underlying mechanism is completely different from the arrhythmias so far? If so, it needs to be demonstrated; if not, is there a method that could reconstruct the activation sequence of a reentrant ventricular tachycardia? Can this method reconstruct the activation-recovery-interval (ARI) distribution in ventricles other than the activation sequence? For treating arrhythmias, localization of the earliest activated site is important for ablation procedure. In addition to cardiac electrical imaging, can we facilitate the process of localization using other techniques?

All of these questions need to be solved and the answers to these questions contribute to the completeness of 3DCEI. In the past 4 years, we have made considerable progress by developing and implementing a new algorithm to reconstruct the activation sequence of reentrant ventricular tachycardia, by developing and applying 3D ARI imaging and by using convolutional neural networks for the localization of ventricular arrhythmias.

1.3 The Organization of this Thesis

This thesis covers some research outcomes we have achieved in noninvasive cardiac electrical imaging and localization of ventricular arrhythmias.

Chapter 2 provides the necessary background knowledge related to this thesis. It covers the introduction to cardiac electrophysiology, ventricular arrhythmias,

electrocardiography (ECG) and body surface potential mapping. Then a brief review of clinical mapping techniques and noninvasive imaging techniques is given. Finally, technical details supporting all the projects of this dissertation research are illustrated to avoid repetitions. This includes forward modeling of cardiac electrical imaging, computer simulation on a realistic anisotropic ventricle model and statistical analysis methods of evaluating performance.

Chapter 3 is a comprehensive study on imaging activation sequences of ventricular arrhythmias by formulating the inverse problem in frequency domain and applying a spatial gradient sparse constraint. To our knowledge, this method is the first one that could reconstruct the activation sequence of a global reentrant ventricular tachycardia. Computer simulation and animal studies were done to evaluate and validate the method.

Chapter 4 demonstrates the capability of 3-dimensional cardiac electrical imaging (3DCEI) in reconstructing the activation-recovery-interval (ARI) distribution in ventricles. Reconstructed ARI distributions were evaluated with the extracted ARI distributions from CARTO system in ten patients.

Chapter 5 introduces a novel method to localize the origins of premature ventricular contraction (PVC) by applying convolutional neural networks to 12-lead ECG. The performance of this method was evaluated under different noise levels and a variety of heart registration errors. Moreover, it was applied to nine PVC patients and obtained a good average localization error around 11 mm.

Chapter 6 summarizes major contributions of the present dissertation research and provides recommendations for future works.

The references and publication list are at the end.

Chapter 2

Background

2.1 Cardiac Electrical Activity

The normal electrical conduction in the heart allows the heart to contract and pump blood to all the organs regularly. Within one cardiac cycle, the electrical impulse generated by the sinoatrial node (SA node) is first propagated to the whole atria and then to the atrioventricular node (AV node), which is located in the interatrial septum. From AV node, the impulse is further conducted through the left and right bundle of His to the respective Purkinje fibers, the endocardium of the apex and finally to the ventricular epicardium. [1] This ordered conduction system in the heart initiates a depolarization wave front that spreads through the myocardium tissues.

The cardiac electrical activity is the result of electrochemical reactions of excitable myocardium cells. [2] A myocardial cell has a negative membrane potential when at rest. If a stimulation is above the threshold, the ion channel will open and allow the ions flow in or out of the membrane. The inflow of sodium ions cause depolarization and the membrane potential will increase dramatically from -90 mV to 0 mV. The repolarization phase is a result of the outflow of potassium ions, and the membrane potential will first decrease slowly and then decrease to the resting potential. This membrane potential change is called action potential.

2.2 Ventricular Arrhythmias

Ventricular arrhythmias are defined as abnormal heart rhythms (arrhythmias) that originate from the lower chambers of the heart (ventricles). The abnormal heart rhythms can be either a very slow heart rate (bradycardia, <60 bpm) or a very fast heart rate (tachycardia, >100 bpm). Sustained ventricular arrhythmias—ventricular tachycardia (VT) and ventricular fibrillation (VF)—are the arrhythmias that last longer than 30 seconds without self-termination and they are the predominant causes of morbidity and sudden cardiac death. Based on the duration, morphology of QRS complexes and clinical characteristics, ventricular arrhythmias could be classified into different categories. [3]

Ventricular tachycardia is one category that covers most classifications and it can be broadly divided into two subcategories depending on the presence or absence of structural heart disease. [4] Focal and reentry are two main mechanisms underlying VT. Idiopathic VT is usually observed in patients without structural heart disease and most of them have a focal origin such as in outflow tracts. [5] For patients with structural heart disease, the most common mechanism of VT is scar-related reentry. [6]

A premature ventricular contraction (PVC) is a type of ectopic beat, in which the heart beat is initiated by an ectopic pacemaker in the ventricles. It is one of the most common ventricular arrhythmias and its prevalence is associated with many factors, such as age, sex, race, and the presence of heart disease. The prevalence of PVC is >6% among 15,792 adults (aged 45-65 years) from the US based on a 2-minute ECG in a large cross-sectional analysis. [7] If not treated in time, the condition of PVC may degenerate into other ventricular arrhythmias such as ventricular tachycardia (VT) and ventricular fibrillation (VF) and finally lead to sudden cardiac death.

Reentry is defined as the electrical circuit looping back upon itself. Reentry happens because of either an anatomical obstacle in the heart with a structural heart disease or a functional conduction block in a normal heart. Myocardial infarction is a type of anatomical obstacles that could generate a reentry because of the excitable gap produced by the tissues in the infarction area. Within the infarction zone, tissues are either electrically unexcitable or with low conduction velocities. This prolongs the time for an excitation wave to propagate once around the circuit (the revolution time). Moreover, once the revolution time exceeds the refractory period along the circuit, the reentry could maintain.

2.3 Electrocardiography and Body Surface Potential Mapping

Considering the heart as an electrical source, the electrical potentials generated by the electrical activity of the heart could propagate through the torso and reach the body surface. If we put electrodes over the body surface, the electrocardiogram (ECG) will be obtained. The 12-lead ECG system is the most popular and widely used noninvasive detection of the cardiac electrical activity in the clinical setting. It is constituted of three bipolar limb leads (lead I to lead III), six unipolar precordial leads (lead V1 to V6) with

reference to the Wilson's Central Terminal, and three segmented unipolar leads (aVR, aVL, and aVF). The waveforms of ECG could give lots of diagnostic information.

It is noted that ECG may not be adequate since the characteristic signals of some cardiac disease arise in the region not covered by 12-lead ECG system. Body surface potential mapping [8] is developed for recording ECG signals over the body surface to get an instant-by-instant spatial distribution of ECG signals. Many experimental and clinical studies have shown that body surface potential mapping has a higher diagnostic power and be more informative. [9]–[11] However, it still doesn't provide the direct information of electrical activities within the heart. In addition, the smearing effect of heart-torso volume conductor [12] makes many electrophysiological events undistinguishable on the body surface that could be observed on the epicardium or within the myocardium.

2.4 Clinical Mapping Techniques

Therapeutic options to treat ventricular arrhythmias include antiarrhythmic drugs, implantable cardioverter-defibrillators (ICDs) and catheter ablation. While antiarrhythmic drugs suffer from the disappointing efficacy and adverse side effects and ICDs are painful and reduce patients' quality of life, catheter ablation emerged as the most common technique nowadays because of its simplicity and safety. Radiofrequency catheter ablation [13] is a minimally invasive procedure that by delivering energy to the sections of the heart who are prone to producing arrhythmias, the arrhythmias are terminated and the patient is treated.

Before applying radiofrequency in the arrhythmogenic area, different endocardial mapping techniques have been used to identify the target of ablation depending on the mechanism of the arrhythmia. For focal VTs, the target of ablation is the point with the earliest activation. Activation mapping techniques such as CARTO® (Biosense Webster, Diamond Bar, CA, USA) and NavX® (Endocardial Solutions, St. Jude Medical Inc., St. Paul, MN, USA) can create a three-dimensional (3D) activation time colored map by assigning an activation time to each measured location sequentially. Simultaneous activation mapping could be done by the EnSite® non-contact mapping system (Endocardial Solutions, St. Jude Medical Inc., St. Paul, MN, USA). This system utilizes a multi-electrode array to record electrical signals from multiple sites. For reentrant VTs,

entrainment mapping is usually considered as a supplement to activation mapping because it is limited when clinical VTs cannot be induced or are hemodynamically unstable. For scar-related VTs, substrate mapping is useful in determining the anatomical substrates that could lead to VTs by creating a 3D amplitude map of local electrogram potentials. Regions with low potentials (<1.5 mV) are considered pathological. [14], [15] Pace mapping could be applied to both focal VTs and reentrant VTs. By comparing the morphology of clinical VTs with that produced by stimulating at a site during sinus rhythm, it is able to locate the origin of a focal VT or any point within the slow-conduction zone in a scar-related VT. It is considered less precise than activation mapping for focal VTs but can serve as a supplement to substrate mapping to delineate a possible isthmus zone.

2.5 Noninvasive Imaging Techniques

The aforementioned endocardial mapping techniques are invasive and limited by their covering area, which makes cardiac electrical imaging technique a promising approach in noninvasively reconstructing activation sequences or action potentials of the whole heart. Noninvasive cardiac electrical imaging is important and significant for understanding the mechanisms of cardiac electrophysiology and for guiding therapeutic treatments of cardiac disorders. By detecting the earliest activated location, it allows the physicians to know the potential area of ablation before inserting a catheter into the heart, which improves the effectiveness and efficiency of catheter ablation and reduces the overall procedure time. By reconstructing action potentials, it could identify regions with low potentials and estimate the extent of myocardial infarction. By reconstructing the activation sequences, it helps in understanding the mechanism of ventricular arrhythmias.

Noninvasive cardiac electrical imaging involves solving the inverse problem of electrocardiography. In the past years, the work in this field can be classified based on different aspects. **(1)** The input could be body surface potentials [16]–[50] or endocardial potentials. [51], [52] Using body surface potentials as input is predominant because of a larger covering area with more electrodes. Using endocardial potentials does not belong to noninvasive cardiac electrical imaging technique by a narrower definition. **(2)** The source model could be a single moving dipole model [17], [23], [33] or equivalent distributed dipole model. [18], [21], [26], [49] Equivalent distributed dipole model was used since the

computational power increased dramatically in the past decade. **(3)** The solution space could be two-dimensional [16], [18], [21], [24], [25], [27], [36], [44] or three-dimensional. [28]–[30], [32], [34], [35], [37]–[43], [45]–[50] Imaging cardiac activities in 3D space or throughout the myocardium is more desirable since cardiac electrical propagation is inhomogeneous and varies across the myocardium. **(4)** The information to formulate a constraint in order to deal with the ill-posed property of the inverse problem could be physiological knowledge [20], [34] or physical knowledge. [18], [26], [49] Physiological knowledge such as the prior knowledge of cardiac electrical activity, fiber orientation and statistical knowledge from body surface potentials could help a lot in solving the inverse problem and achieving a global optimum. But it is also limited by incorporating into the physiological knowledge when the state of the heart is complicated or could not be evaluated accurately. Physical knowledge includes the geometry of the heart and the physical relationship between cardiac sources and body surface electrodes. It is robust in the sense of its applicability. However, when it requires to identify the extent of infarction or slow-conduction zone, physiological-knowledge-based approach [28], [35], [39], [48] has less limitations than the physical-knowledge-based approach. [50] **(5)** The unit of solution could be time (activation sequence) [21], [26], [27] or potential (endocardial or epicardial potential [16], [18], [44]and transmural potential [29], [34], [38]) Activation sequence directly locates the earliest activated site which has the minimal value in the solution and reflects electrical propagation pathways of ventricular arrhythmias. On the other hand, more parameters could be derived from the reconstructed potentials and usually the amplitude of the potential is a marker for identifying infarction or slow-conduction zone. **(6)** The norm of the constraint could be L2-norm [18], [26], [44], L1-norm [45], [49] or a norm in between. [41] L2-norm is based on the minimization of energy resulting from the consensus that a stable state usually possesses the least energy. L1-norm is usually associated with sparsity. Sparsity could appear either in space or in time depending on which property is pursued. To solve the inverse problem, a problem with L2-norm constraints is easy to solve and is guaranteed with a global optimum. However, a problem with L1-norm or other norms is hard to find an optimum and requires some special algorithms to search the solution space and find a solution. The solution will be smooth if

it is L2-norm, and sparse if it is L1-norm. A norm between 1 and 2 will result in a smoothness in between these two.

2.6 Forward Modeling of Cardiac Electrical Imaging

Based on the bi-domain theory [53]–[55], the discrete cellular architecture can be represented by a macroscopic continuum model which consists of two domains: the intracellular and extracellular domain. These two domains are connected by transmembrane currents flowing in between across a theoretical membrane with no thickness. Assuming a quasi-static condition, the electrical field within the volume conductor is governed by:

$$\nabla \cdot [(G_i + G_e)\nabla \emptyset_e] = \nabla \cdot (-G_i \nabla \emptyset_m) \qquad (2.1)$$

where G_i and G_e are intracellular and extracellular conductivity tensors respectively, $\emptyset_e$ is the extracellular potential and $\emptyset_m$ is the transmembrane potential. If we define equivalent current density to be $\vec{J}_{eq} = -G_i \nabla \emptyset_m$, then the above equation can be rewritten as:

$$\nabla \cdot [(G_i + G_e)\nabla \emptyset_e] = \nabla \cdot \vec{J}_{eq} \qquad (2.2)$$

Thus, $\vec{J}_{eq}$ can be the equivalent cardiac sources for generating cardiac electrical activities. To model the distributed current sources, the whole ventricular myocardium is discretized into *N* grid points. An orthogonal triple dipole is placed at each grid point to represent local vector field with an arbitrary direction.

According to the analytical derivation [56], at any time, the electrical potential at a given point on the torso surface is a linear superimposition of all the potential fields generated by cardiac sources at that time. By applying BEM theory after the tessellation of relevant surfaces (torso, lungs and epicardium), this linear relationship is also reflected in the discrete matrix equation:

$$\emptyset_b(t) = LJ(t) \qquad (2.3)$$

where $\emptyset_b(t)$ is a *M×1* vector of body surface potentials at *M* electrode positions at time t and $J(t)$ is a *3N×1* vector of the equivalent current density at *N* source locations at time t.

L is an $M \times 3N$ transfer matrix with the lead field between one electrode and one cardiac source is a 1×3 vector.

So formulating an equation that builds a relationship between source activities and measured signals is called the forward modeling. And given measured signals and the transfer matrix, finding a solution that both approximates the measured signals after being multiplied with the transfer matrix — minimize the difference between the left side and the right side of Eq. (2.3) — and satisfies some physiological (or physical) constraints depending on which desirable properties to pursue is called solving the inverse problem. Forward modeling and solving the inverse problem are associated closely and interact with each other. In some cases, the former determines what algorithm to use in the latter. And in other cases, pursuing one property in the constraint will require a different forward modeling. These two concepts are not limited to the cardiac electrical imaging field, and they belong to a general field of source imaging.

2.7 Computer Simulation on a Realistic Anisotropic Ventricle Model

A cellular automaton heart model simulated the ventricular excitation. As described in the paper by He et al. [22], heart geometry was constructed from CT images of a human subject and discretized into around 38,000 cellular units with a side length of 1.5 mm. Then a generalized ventricle conduction anisotropy was incorporated into the model. The myocardial fiber orientations rotated counterclockwise over 120° from the outermost layer (epicardium, -60°) to the innermost layer (endocardium, +60°) with equivalent increment between the consecutive layers. The conduction velocity along the fiber was 0.6 m/s, and 0.2 m/s transverse to the fiber, respectively. In addition, the longitude intracellular conductivity was set as 0.3 S/m and the transverse intracellular conductivity was 0.075 S/m, respectively. The action potential and the vector of local fiber orientation were set individually over all the ventricular cellular units. The equivalent current-dipole density of each unit was computed as the product of the myocardial conductivity tensor and the spatial gradient of instantaneous transmembrane potential. Each dipole has three orthogonal components. Finally, cellular units were further grouped into 3,887 dipoles according to their segment number. To simulate a single-site pacing, a dipole is chosen to be the starting point of a cardiac electrical propagation in the heart. This is a single beat activation model

and the time resolution of the generated current density is one millisecond. This ventricle current-dipole model was used previously in the simulation study of a 3-dimensional cardiac imaging technique [26], [49]. It will be used for the computer simulation in this thesis.

2.8 Statistical Analysis

To evaluate the performance of an imaging technique for the reconstruction of activation sequence in the heart, three parameters are usually calculated. The correlation coefficient (CC) and relative error (RE) were computed to quantify the agreement of the overall activation pattern. Localization error (LE) was computed to evaluate the targeting performance of the proposed method. CC, RE and LE are defined as:

$$\mathrm{CC} = \frac{\sum_i (AT_i - \overline{AT}) \cdot (MT_i - \overline{MT})}{\sqrt{\sum_i (AT_i - \overline{AT})^2} \cdot \sqrt{\sum_i (MT_i - \overline{MT})^2}} \qquad (2.4)$$

$$\mathrm{RE} = \sqrt{\frac{\sum_i (AT_i - MT_i)^2}{\sum_i {MT_i}^2}} \qquad (2.5)$$

$$\mathrm{LE} = \|S_I - S_M\| \qquad (2.6)$$

where AT_i and MT_i represent the imaged and measured (or simulated) activation time at i^{th} cardiac source, $\overline{AT}$ and $\overline{MT}$ are the average of the two sequences, and S_I and S_M are the spatial locations of imaged and measured earliest (or latest) activation time sites respectively.

Chapter 3

Noninvasive Activation Imaging of Ventricular Arrhythmias (Focal and Reentry)

3.1 Introduction

As discussed in Section 2.1, ventricular arrhythmias are classified into different categories from a variety of perspectives. Here, we look at ventricular arrhythmias from another angle and classify ventricular arrhythmias into two categories based on its periodicity. Referring to the international consensus document on VT/VF ablation [57], a periodic arrhythmia can be non-sustained VT or sustained VT (Duration Classification), can be monomorphic VT, an episode from multiple monomorphic VT, a segment of pleomorphic VT or ventricular flutter (Morphology of QRS complexes Classification), and can be clinical VT, incessant VT, repetitive monomorphic VT or an episode of VT storm (Clinical Characteristics Classification). A periodic arrhythmia covers both focal VT and scar-related reentry regarding the underlying mechanism of VT. The common property we are looking for is a relatively stable VT originating from the same origin or generated by the same reentrant circuit. The body surface ECGs of periodic arrhythmias listed above can be the direct input to our proposed novel imaging algorithm. We will show later that ECGs of VT as short as 2-3 seconds could produce satisfying results given the heart rate is high enough to produce an adequate frequency resolution in a myocardial infarction swine model.

On the other hand, VTs with dynamically changing QRS configurations and VF, which has a very chaotic morphology, are aperiodic and cannot be the direct input to our imaging algorithm. This is understandable since we lose the time resolution by formulating and solving the problem in the frequency domain. The more stable, the better. The proposed imaging algorithm cannot be applied to premature ventricular complexes (PVC) at first thought because the presence of an isolated complex. However, by concatenating the same PVC beat multiple times, we could obtain an artificial VT train. Concatenation is applicable to other single beats that are extracted from VTs. We applied concatenation when we tested

the algorithm via computer simulation. Since concatenation is feasible, we could make a final claim that our proposed novel imaging algorithm cannot be applied when the VTs are generated by continuing changing reentrant circuits or when VF occurs. Given the low incidences of the above cases, our proposed imaging algorithm will be able to reconstruct activation sequences in a majority of ventricular arrhythmias.

On a higher level, reconstructing activation sequences by cardiac electrical imaging technique is a type of source imaging. In the heart, source imaging aims to find the site with the earliest activation time. In the brain, source imaging aims to locate the region that initiates brain activities such as epilepsy. Brain activities are divided into different frequency bands, so that a method taking into multiple dimensions (space, time or frequency) will produce better results. To combine time and frequency, short-time Fourier transform (STFT) is incorporated into the inverse problem. [58] And recently, STOUT (spatiotemporal unifying tomography) [59] was proposed which combined space, time and frequency. Besides combinations of different dimensions, solving the inverse problem totally in the frequency domain [60], [61] allows us to focus on a specific frequency band. The linear relationship between sources and electrodes still holds after the Fourier transformation on both sides. The real and imaginary parts were solved independently by using a weighted minimum norm approach. Source strength was estimated afterwards. In the heart, most works formulated and solved the inverse problem in the time domain. Recently, a temporal-sparse algorithm [49] was proposed to take the time dimension into consideration and achieved a better temporal resolution. However, to our knowledge, there does not exist any method that solves the cardiac inverse problem totally in the frequency domain.

Thus, we proposed a physical-knowledge-based method on projected edge dipole model (derived from equivalent distributed dipole model) to reconstruct activation sequences for periodic arrhythmias from body surface potentials noninvasively. Based on the above discussion, the imaging approach we proposed—SSF (Spatial gradient Sparse in the Frequency domain)—is novel in five folds. **(1)** It takes the complex number after Fourier transform as a whole and solves real and imaginary parts together. **(2)** It imposes a weighted gradient sparsity in space as the constraint. **(3)** The activation time is related with

the phase (calculated from real and imaginary parts of the solution). There is no need to apply peak criteria [26] in the time course to determine the activation time for each source. **(4)** A projected edge dipole model derived from the distributed rotating dipole model is developed to make the proposed algorithm feasible. **(5)** This is the first time that a 3D reentrant circuit throughout the ventricles could be reconstructed noninvasively by an imaging method. Among the current invasive mapping techniques, although Ensite® could record signals from multiple sites in the reentrant VT, it is limited by the number of the electrodes and their total covering area in one chamber of the ventricles.

3.2 Methods

3.2.1 Equivalent Current Density on Edge in a Tetrahedron Model

We have introduced the forward modeling on a distributed current dipole model in Section 2.4, and an orthogonal triple dipole represents the local vector field of equivalent current density with an arbitrary direction. When a periodic cardiac activity occurs, a myocardial cell is activated periodically. Its transmembrane potential fluctuates in a given frequency and so does the magnitude of equivalent current density. To incorporate this periodicity into our imaging scheme, constraining directly on the magnitude of an orthogonal triple dipole would give rise to the complexity of solving the inverse problem and limit the possible transformation that could be applied to the formulation. Therefore, we propose a new tetrahedron model with each edge center representing the equivalent current density.

A Delaunay triangulation transformed the N distributed dipoles into tetrahedrons. The long edges that connect two dipoles farther than the threshold were detected and deleted since their centers were not confined to the ventricular myocardium. The threshold was estimated by calculating distances between each dipole and all the other dipoles. After removing tetrahedrons with long edges, the edges that do not belong to any remaining tetrahedrons were further deleted. Therefore, a clean tetrahedron model was created and it was plotted for a manual check that there was no cavity in the model; otherwise, a looser threshold would be chosen to generate a new tetrahedron model.

Since the edge centers serve as the new current sources, the transfer matrix needs to be updated as well. For the k^{th} edge that connects i^{th} dipole and j^{th} dipole, the lead field between this edge and m^{th} body surface electrode is defined as:

$$Le_{mk} = (\left|\vec{e}_k \cdot \frac{L_{mi}}{|L_{mi}|} + \vec{e}_k \cdot \frac{L_{mj}}{|L_{mj}|}\right|)/2 \quad (3.1)$$

where Le_{mk} is the edge lead field between m^{th} electrode and k^{th} edge, $\vec{e}_k$ is the spatial vector between two dipoles, L_{mi} is a 1×3 vector of the dipole lead field between m^{th} electrode and i^{th} dipole and L_{mj} is the dipole lead field between m^{th} electrode and j^{th} dipole. Because the absolute value of vector projection is used, the direction of $\vec{e}_k$ does not matter and Le_{mk} is a non-negative value.

For a tetrahedron model, rewrite Eq. (3.1) as:

$$\Phi = L_E J_E \qquad (3.2)$$

where Φ is an $M \times 1$ vector of body surface potentials at M electrodes, J_E is a $K \times 1$ vector of equivalent current density at K edge centers, and L_E is an $M \times K$ transfer matrix for tetrahedron model.

3.2.2 Forward Modeling and Spatial Gradient Sparse in Frequency Domain

A periodic signal is characterized by its main oscillating frequency and phase in the frequency domain. When the ventricular myocardium is activated in sequence, there is a time delay in the time domain and a phase shift in the frequency domain. Based on the linearity of Eq. (3.2) and time shift property of Fourier transform, Eq. (3.2) can be transformed into the frequency domain and the phase of each edge current source corresponds to its activation time.

Expand Eq. (3.2):

$$\begin{bmatrix} \phi_1(t) \\ \phi_2(t) \\ \vdots \\ \phi_M(t) \end{bmatrix} = \begin{bmatrix} Le_{1,1}Je_1(t-t_1) + Le_{1,2}Je_2(t-t_2) + \cdots + Le_{1,K}Je_K(t-t_K) \\ Le_{2,1}Je_1(t-t_1) + Le_{2,2}Je_2(t-t_2) + \cdots + Le_{2,K}Je_K(t-t_K) \\ \vdots \\ Le_{M,1}Je_1(t-t_1) + Le_{M,2}Je_2(t-t_2) + \cdots + Le_{M,K}Je_K(t-t_K) \end{bmatrix} \quad (3.3)$$

Apply Fourier transform to Eq. (3.3) and substitute into the main oscillating frequency ω_0:

$$\begin{bmatrix} F_{\phi 1}(\omega_0) \\ F_{\phi 2}(\omega_0) \\ \vdots \\ F_{\phi M}(\omega_0) \end{bmatrix} = \begin{bmatrix} Le_{1,1}F_{Je1}(\omega_0)e^{-j\omega t_1} + Le_{1,2}F_{Je2}(\omega_0)e^{-j\omega t_2} + \cdots + Le_{1,K}F_{JeK}(\omega_0)e^{-j\omega t_K} \\ Le_{2,1}F_{Je1}(\omega_0)e^{-j\omega t_1} + Le_{2,2}F_{Je2}(\omega_0)e^{-j\omega t_2} + \cdots + Le_{2,K}F_{JeK}(\omega_0)e^{-j\omega t_K} \\ \vdots \\ Le_{M,1}F_{Je1}(\omega_0)e^{-j\omega t_1} + Le_{M,2}F_{Je2}(\omega_0)e^{-j\omega t_2} + \cdots + Le_{M,K}F_{JeK}(\omega_0)e^{-j\omega t_K} \end{bmatrix} \quad (3.4)$$

Thus, in the frequency domain, Eq. (3.2) is expressed as:

$$F_{\emptyset}(\omega_0) = L_E F_{J_E}(\omega_0) \quad (3.5)$$

where $F_{\emptyset}(\omega_0)$ is an $M \times 1$ complex vector and $F_{J_E}(\omega_0)$ is a $K \times 1$ complex vector. Because we only care for the main oscillating frequency in the heart, ω_0 is omitted in the following equations and it is determined by detecting the frequency with the maximum power in the power spectrum except the direct current component.

Suppose we extract amplitude and phase from the main frequency ω_0, in the time domain $Je_i(t - t_i)$ can be expressed as $A_i \cos(\omega_0 t - t_i)$, and its Fourier transform will be:

$$F_{J_{ei}}(\omega_0) = F\{A_i \cos(\omega_0 t - t_i)\}(\omega_0) = \{e^{-j\omega_0 t_i} \cdot \frac{1}{2} A_i[\delta(\omega - \omega_0) + \delta(\omega + \omega_0)]\}(\omega_0) = e^{-j\omega_0 t_i} \cdot \frac{1}{2} A_i = e^{-j\varphi_i} \cdot \frac{1}{2} A_i \quad (3.6)$$

$$\text{Phase } \varphi_i = \omega_0 t_i \propto t_i \; for \; all \; i = 1 \cdots K \quad (3.7)$$

From Eq. (3.7), the phase of the complex vector $F_{J_E}(\omega_0)$ is proportional to the time delay in the activation sequence.

Starting from the earliest activated site to the latest activated site, the time delay t_i ranges from 0 to T (cycle length of the periodic cardiac activity), and the phase shift is from 0 to 2π. In MATLAB, the phase is constrained to the range from –π to π. Because of MATLAB convention, the actual phase shift is from 0 to –π, then π to 0, and this corresponds to the original phase shift range of 0 to 2 π. Hence, the sudden change between –π and π always exists. In 3-dimensional space, this results in a spatial gradient sparse of

phase in the myocardium, which could be utilized as a constraint in the reconstruction of activation time.

3.2.3 Weighted Spatial Gradient Sparse Reconstruction

Eq. (3.5) formulates a forward problem that connects distributed edge current sources with body surface potentials in the frequency domain. Given body surface measurements and the lead field, solving the equivalent current density cannot be done by a direct matrix inversion because this is a highly ill-posed problem. Regularization needs to be added to obtain a unique and stable solution, and the constraint terms are usually based on the physiological property of the heart [19], [34] or the physical property of the cardiac model. [26], [49] Solution that achieves the minimum energy is considered as feasible and stable; hence it is widely used in cardiac electrical imaging. [18], [27] In our proposed method, a weighted spatial gradient sparse is applied:

$$F_{J_E} = \arg\min_{F_{J_E}}\left(\left\|L_E F_{J_E} - F_\emptyset\right\|_2^2 + \lambda\left\|WGF_{J_E}\right\|_1^1\right) \qquad (3.8)$$

$$W_{1,k} = \frac{1}{\sqrt{\sum_{j=1}^{M} L_{E(j,k)}^2}} \; for\ all\ k = 1\ \cdots K \qquad (3.9)$$

$$G_{k,k} = 1 + r, G_{k,j} = \begin{cases} -1, j \in R \\ 0, j \notin R \end{cases} \quad k, j = 1 \cdots K \qquad (3.10)$$

W is a depth weighting matrix to balance the deep sources in the heart model, G is a numerical first order gradient matrix, R is a set including all the neighboring current sources' indices and r is the number of elements in set R. Neighboring sources are determined by calculating spatial distances between one source and all the other sources and sorting them in an ascending order. λ is the regularization parameter which can be determined by L-curve method. [62], [63] r determines how wide the smooth region will be in the final solution, and λ balances between the residual term and the spatial sparse term. They are both data-driven. For the noisy data, a small r and λ will be very sensitive to the noise. Therefore, a larger r and λ is desirable for experimental data and a smaller r and λ is suitable for simulation data. The range of them is usually from 1 to 10. Also, r should not be too large to lose the sparse property in the solution.

It is worthy of noticing that the spatial gradient sparse constraint is applied to F_{J_E} which is a complex vector, not to the phase of F_{J_E}. This is because the mathematical expression of phase is nonlinear and will render the problem to a non-convex problem. A non-convex problem is hard to solve and requires special algorithms to deal with. Therefore, the current formulation Eq. (3.8) to (3.10) formulates a convex constrained problem, which can be solved with CVX, a MATLAB package, specialized in solving convex programs. [64] When F_{J_E} is obtained, phase is easy to calculate. In addition, according to the above discussion, after flipping the phase from 0 to $-\pi$ and π to 0 to the range of 0 to 2π, the activation time is computed by multiplying the cycle length T divided by 2π and the 3D activation sequence of the reentrant circuit is reconstructed.

3.2.4 Computer Simulation of Focal Ventricular Tachycardia

To simulate a focal VT train, single-site pacing simulation on a realistic anisotropic ventricle model was used (as described in Section 2.5). A tetrahedron model was built upon this dipole model, and the equivalent current density on each edge was calculated, similar as in Eq. (3.1), by a spatial projection of the two dipoles' components that are connected with this edge. In total, 12 pacing sites were selected based on the anatomical structure of the ventricles, namely in basal posterior (BP), basal septum (BS), basal left wall (BLW), basal right wall (BRW), basal anterior (BA), middle septum (MS), middle posterior (MP), middle left wall (MLW), middle right wall (MRW), middle anterior (MA), apical anterior (AA) and apical posterior (AP). For each single-site pacing simulation, the time courses of all the current density on edge were plotted to determine the beginning and ending time of a single-beat activation. The time segment of the activation was extracted and concatenated 100 times to form a chain. The whole series of current density were filtered by a zero-phase bandpass filter between 1 Hz and 10 Hz. Since VT is defined as with a heart rate higher than 120 bpm, we did down sampling to the filtered current density to represent a similar heart rate.

The boundary element model of a heart-torso model was built by using a commercial software (Curry 6.0, Neuroscan, North Carolina, USA) based on the torso and lungs segmented from a standard high-resolution male torso MRI images (ViP V2.0 IT'IS Foundation, Zürich, Switzerland). Two hundred and eight body surface electrodes recorded

from a human subject were placed on the front and back of body surface, and were registered with the heart-torso model. The lead field between dipoles and electrodes was transformed to the lead field between edge sources and electrodes by Eq. (3.1). The body surface potentials of a focal VT train were generated by multiplying the train of current density with the lead field.

Gaussian white noise of various SNR levels (5, 10, 20 and 40 dB) were added to the forward calculated body surface potentials to simulate ECG signals collected in a clinical setting. Then we applied Fourier transform to the final simulated body surface potentials of a focal VT train to calculate the power across different frequencies, and the main oscillating frequency was determined by detecting the frequency with the maximum power except direct current component. Eq. (3.8) to (3.10) were employed to solve the inverse problem in the frequency domain and the activation sequence was reconstructed accordingly. The schematic diagram of computer simulation is presented in Fig. 1.

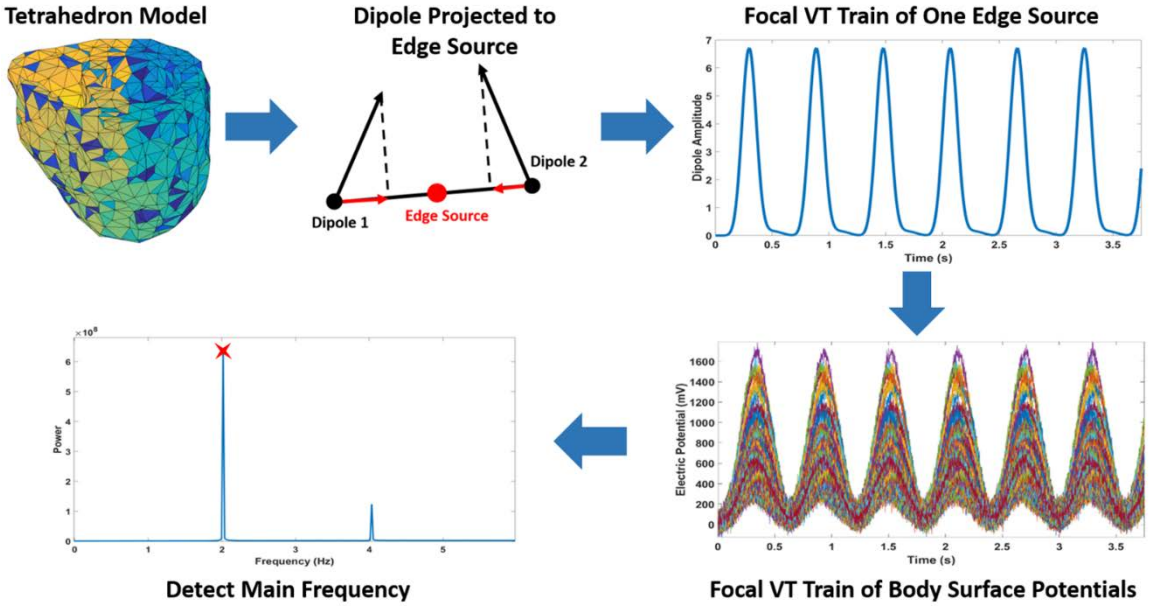

Figure 1 Schematic diagram of computer simulation of focal ventricular tachycardia. VT = ventricular tachycardia.

3.2.5 Application to Reentrant Ventricular Tachycardia in a Swine Model

To apply the proposed method to reentrant VT, four female pigs were studied under a protocol for simultaneous body surface potential mapping and 3D intracardiac mapping.

[65], [66] The study protocol was approved by the Institutional Animal Care and Use Committee at University of Alabama at Birmingham. The study flowchart is shown in Fig.2. Left anterior descending (LAD) artery occlusion was done 2 months and a week before the mapping study and the occlusion time duration was 150 minutes. Therefore, this is a late myocardial infarction swine model. After a month, the enchocardiography study was performed to assess the states of the pigs. Then one week before the mapping study, anatomical MRI and delay-enhanced MRI images were obtained to construct the swine heart-torso model and for the identification of myocardial fibrosis regions respectively (Panel B in Fig. 3).

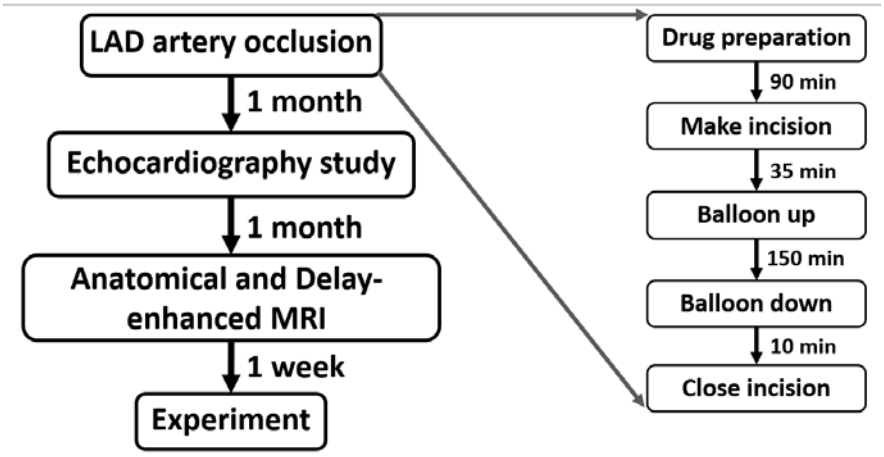

Figure 2 Swine study flowchart. CT = computational tomography, LAD = left anterior descending, MRI = magnetic resonance imaging.

On the day of mapping, 128 body surface electrodes were first placed on the front chest and back of the pig to record body-surface potentials at a sampling rate of 1 kHz. The locations of body surface electrodes were digitized using an electromagnetic 3D digitizer (Fastrak, Polhemus Inc., Colchester, VT, USA). Then the catheter was inserted for pacing. After several minutes of signal recording with adequate signal quality, the heart was exposed via median sternotomy. Up to 70 transmural plunge-needle electrodes were inserted into the left ventricle, the right ventricle and the septum. Each plunge-needle electrode contains 3 to 6 unipolar channels with an inter-channel distance of 1 mm. The number of channels that each plunge-needle electrode contained was recorded in a notebook. The plunge-needle electrodes were more densely placed near the myocardial infarction substrates. We sutured the chest, thus the unipolar electrograms were recorded

simultaneously with body surface potentials in a closed-chest condition (Panel D in Fig. 3). Rapid single-site pacing and burst pacing was done to induce reentrant VT in the swine heart.

After the mapping study, the heart was excised with all the plunge-needle electrodes and pressure perfused in formalin for at least 12 hours. Then the heart was flushed under water and used for digitization of plunge-needles. Each plunge-needle was replaced by a color-coded tubing (Panel G in Fig. 3). We digitized the root and the tip of each tube to get an accurate location and direction of each plunge-needle.

The ventricle geometry and torso were segmented from anatomical MRI images by a commercial software (Curry 6.0, Neuroscan, North Carolina, USA) and the body surface electrodes were registered to the torso surface based on several anatomical landmarks (Panel C in Fig.3). The BEM model was built to relate body surface electrodes with distributed cardiac sources. A long segment of body surface potentials with sustained reentrant VT (Panel E in Fig.3) was used for imaging the reentrant circuit. Principle Component Analysis (PCA) was used for extracting the main components with SNR higher than 1 and for further filtering signals after a bandpass filter of 1 and 30 Hz. Finally, a 3D activation sequence was reconstructed by the proposed method (Panel F in Fig. 3).

Since intracardiac mapping results were used for the validation and served as a golden standard of the activation sequence, intracardiac electrograms of several stable reentrant VT beats were analyzed. After bandpass filtering the unipolar signals, the first derivative was calculated for each channel. The time with the maximum negative first derivative was detected as the activation time automatically. By combining the activation time with the positions of plunge-needle electrodes, the 3D activation time map of a reentrant VT beat was constructed (Panel H in Fig. 3). Finally, the plunge-needle electrodes were registered with the ventricle model and the activation time was interpolated spatially to the ventricle model to obtain a 3D intracardiac activation time map (Panel I in Fig. 3).

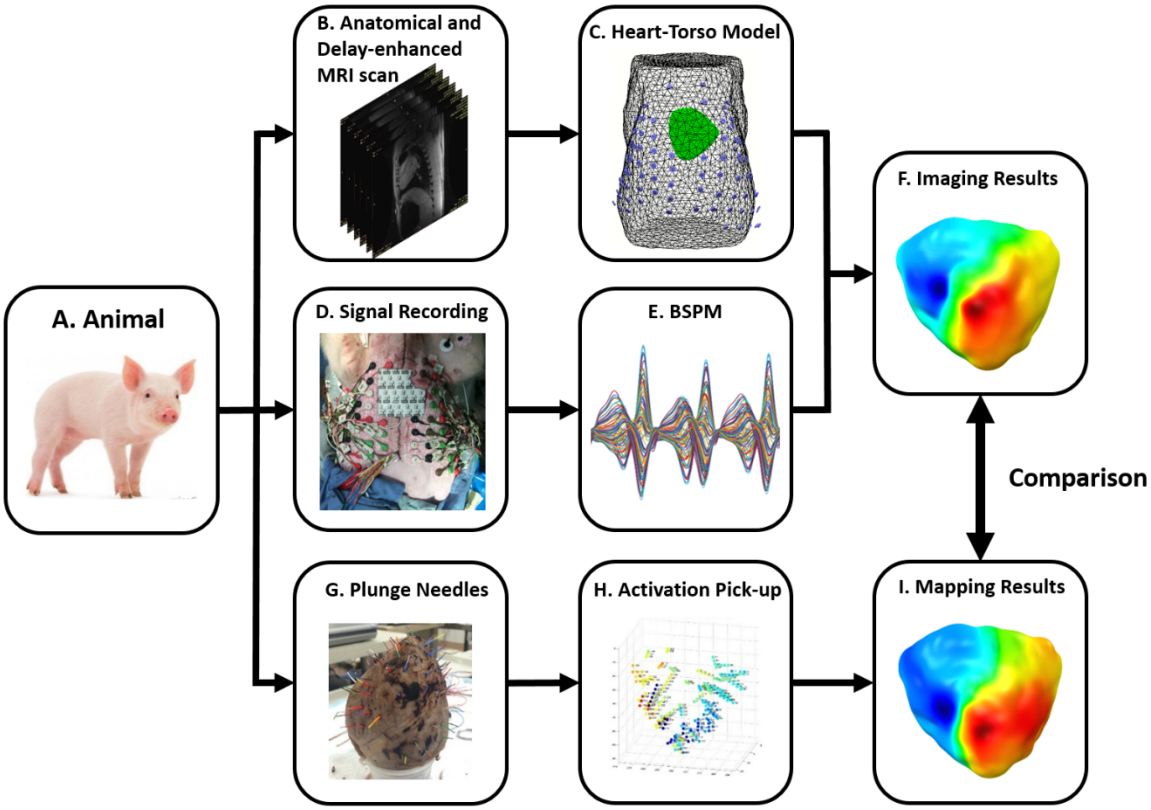

Figure 3 Schematic diagram of swine study. A: experimental animal. B: Anatomical and delay-enhanced MRI for the construction of heart-torso model and the identification of infarction area. C: Heart-torso model with body surface electrodes registered with the body surface. D: Simultaneous body surface recording and intracardiac recording. E: BSPM, the recorded body surface potential maps. F: Imaging results by using the proposed imaging method. G: Excised heart with color-coded tubing replacing plunge-needle electrodes. H: Pick up activation from each unipolar channel. I: Interpolated intracardiac activation time map.

3.2.6 Statistical Analysis

As described in Section 2.6, three parameters were calculated: CC, RE and LE. For computer simulation of focal VT, the evaluation was made between the simulated activation sequence and the imaging activation sequence. In the time domain, we have proposed two methods to localize the origins of PVC or focal VT before: one was based on the weighted minimum norm (WMN) [26]; the other introduced temporal sparse into the formulation. [49] Considering the computational effort, we compared the imaging performance of the proposed method with that of the WMN on the same edge source model. For the WMN method, a single focal VT beat was taken out for the imaging analysis. It

was further evaluated with the simulated activation sequences to get imaging statistics. For the animal experiment of reentrant VT, the evaluation was made between the measured intracardiac activation sequence and the imaged activation sequence.

3.3 Results

3.3.1 Computer Simulation of Focal Ventricular Tachycardia

Table 1 summarizes the imaging statistics of WMN and SSF (Spatial gradient Sparse in the Frequency domain, the proposed method) under different noise levels. As SNR decreases, the performance of WMN declines. However, SSF manages to maintain the good performance unaffected by the noise level. The average CC and LE of 12 single-site pacing simulations are also plotted in the top row of Fig. 4. As for RE, there is no significant difference between the two methods. The RE among different noise levels varies less in SSF than that of WMN. This is due to how we calculated the activation time in SSF. The cycle length of a beat was first determined from the butterfly plot of body surface potentials. Then the phase of SSF with a range of 0 to 2π was multiplied by this cycle length to transfer it into the activation time. Therefore, there was no time shrinkage in SSF. Two factors that influence the value of RE: shape of distribution and the absolute error. SSF with no time shrinkage has less variation in the absolute error so that it also varies little in the value of RE.

Table 1 Imaging Statistics of Computer Simulation

SNR	**CC (%)**		**LE (mm)**		**RE (%)**	
Method	WMN	SSF	WMN	SSF	WMN	SSF
40 dB	88.17±10.83	91.67±7.30	6.0±2.8	4.5±2.2	23.67±6.08	19.42±5.38
20 dB	87.50±10.50	91.67±8.07	7.0±2.9	4.9±2.4	20.58±5.48	21.67±5.07
10 dB	84.92±11.52	90.83±8.91	7.9±3.2	5.3±2.7	19.92±4.98	19.00±4.51
5 dB	83.08±12.10	89.92±9.95	10.2±3.1	5.6±3.2	18.83±4.99	18.75±4.75

CC = correlation coefficient, LE = localization error, RE = relative error, SNR = signal-to-noise ratio, SSF = spatial sparse in frequency domain method, WMN = weighted minimum norm method.

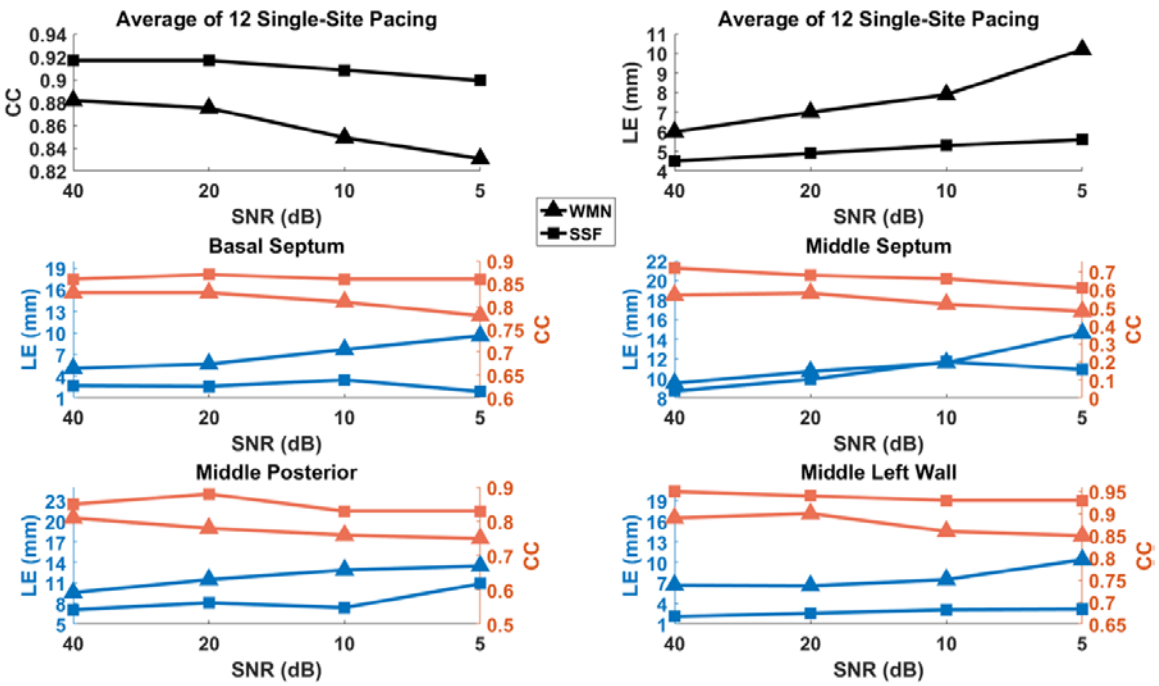

Figure 4 Imaging statistics between SSF and WMN in focal VT simulation. The top row shows the average CC and LE of all the 12 pacing sites. The second and bottom rows present four specific cases that SSF has improved the imaging performance significantly. The triangle mark stands for the WMN method, and the square mark indicates the SSF method. The CC is plotted in orange lines and LE is shown in blue lines.

Among the 12 single-site pacing simulations, four cases are considered difficult and usually have low CCs and LEs: basal septum (BS), middle septum (MS), middle posterior (MP) and middle left wall (MLW). Their imaging statistics are shown in the middle and bottom rows in Fig.4, and the 3D activation sequences are presented in Fig.5. For the first two cases, the difficulty comes from the pacing source lying in the middle region of the heart. On the body surface, the initiation part of the excitation is almost cancelled out by the cardiac electric propagation along two opposite directions. Therefore, the signal is very weak on the body surface, and is hard to be seen by the imaging process. This is the reason why the activation time maps of BS and MS target the earliest activation sites to the sites that are a little bit late in time than the true earliest activation site. WMN tended to assign a single source while SSF was able to obtain a balance in space as shown in the middle column of BS and MS in Fig. 5. When calculating the earliest activation site, this spatial balance led to a smaller LE and a higher CC. Since the left ventricle is remoter

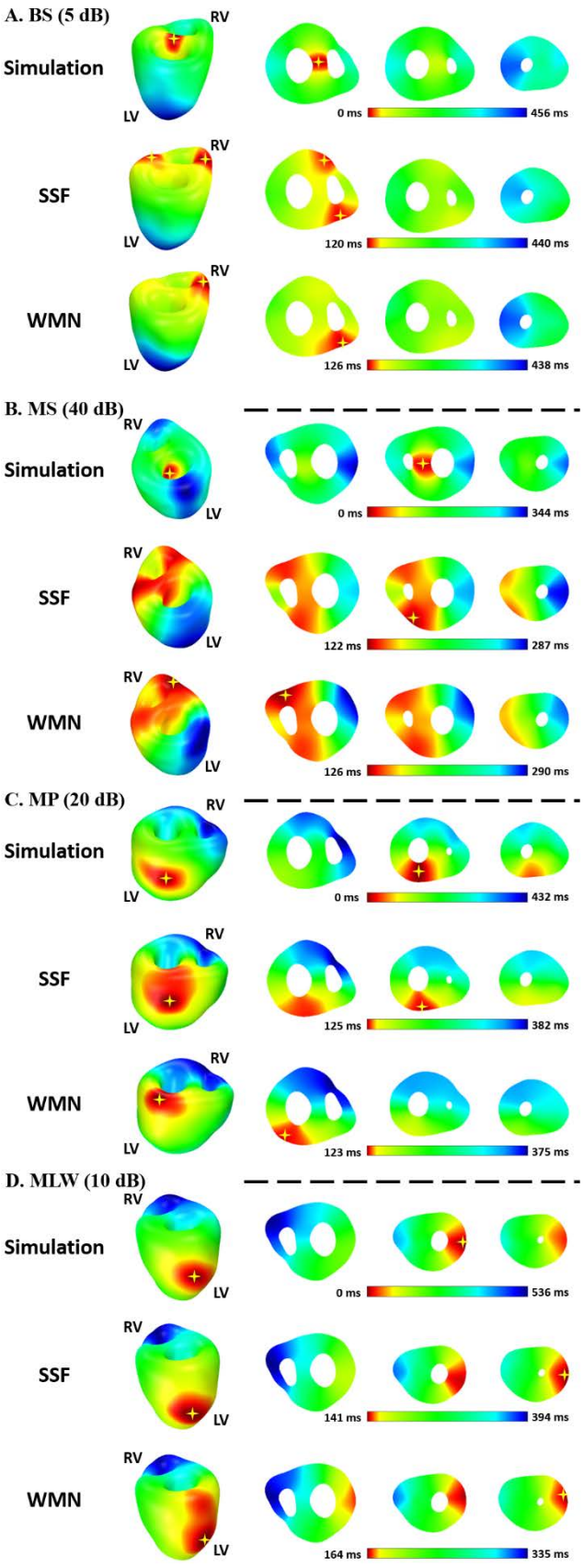

from the front body surface than the right ventricle anatomically in human, pacing source in MP or MLW is considered as a deep source and would be hard to detect. This is where SSF outperformed WMN. Both CC and LE were improved by using SSF. The imaging results are presented in the bottom two rows in Fig. 5. The color bars were the same in the imaging results of SSF and WMN. On general, SSF performs better than WMN and SSF improves the performance the most in these four cases.

Figure 5 Activation time maps of four focal ventricular tachycardia simulations. The pacing sites are on the left with SNR levels underneath. The 3D simulated activation sequences are depicted in the first column. The activation sequences reconstructed by SSF method and WMN method are listed in the second and the third columns respectively. The earliest region in each activation sequence is denoted by a yellow star. All the maps are color coded from red to blue with red representing the earliest activation time and blue for the latest activation time. BS = basal septum, MLW = middle left wall, MP = middle posterior, MS = middle septum, LV = left ventricle, RV = right ventricle.

3.3.2 Reentrant Ventricular Tachycardia in a Swine Model

The physiological statistics of the four pigs are demonstrated in Table 2 including the average infarct extent estimated from delay-enhanced MRI images by experts. It was observed that the blood pressure was higher after the LAD occlusion than that of the healthy state. This was because of the poor circulation that occlusion brought in. Swine 1 had the least infarct extent and the highest ejection fraction rate. On average, the weight of the four pigs is 57.8 ± 4.0 kg.

Table 2 Physiological Statistics of Swine

	Weight (kg)	**BP_H** (mmHg)	**BP_E** (mmHg)	**EF** (%)	**EDV** (ml)	**ESV** (ml)	**AIE** (%)
Swine 1	53.4	82/46	110/66	48.6	89.6	46	8.17
Swine 2	63.1	92/57	122/80	44.4	90.7	50.4	18.7
Swine 3	57.9	61/34	107/76	30.9	134.7	93	17.2
Swine 4	56.8	97/60	127/76	42.3	139.8	80.6	10.9

AIE = average infarct extent; BP_E = blood pressure during the experiment after left anterior descending artery occlusion; BP_H = blood pressure in the healthy state; EDV = end diastolic volume; EF = ejection fraction; ESV = end systolic volume.

Table 3 summarizes the imaging statistics. In total, four long stable reentrant VTs were recorded and analyzed. We did not observe any reentrant VT induced by programmed stimulation in Swine 1, which may be due to its low infarct extent. Two reentrant VTs in Swine 2, one in Swine 3 and one in Swine 4 were successfully induced by stimulation pacing. They were recorded by the intracardiac recording system and by the body surface electrodes simultaneously. We compared the imaged activation sequences with those obtained from the intracardiac unipolar electrograms. The average CC is 88.00 ± 4.83 %, the average RE is 0.23 ± 0.03, the average LE of the earliest activated site is 6.3 ± 1.9 mm and the average LE of the latest activated site is 6.3 ± 3.4 mm. Two reentrant VTs in Swine 2 were more stable compared to the other two reentrant VTs, therefore a longer segment of body surface signals were used for analysis. The main oscillating frequency was estimated from the power spectrum of the analyzed body surface signals (Middle column in Fig. 7), and on average, ω_0 is 5.12 Hz which is equal to 307 bpm (beats per minute).

Table 3 Imaging Statistics of Reentrant VT in a Swine Model

Reentry	Needle	Channel	CC	RE	LE_E (mm)	LE_L (mm)	ω_0 (Hz)	t (s)
S2RVT1	71	257	0.90	0.20	8.5	8.3	4.51	17.7
S2RVT2	71	257	0.88	0.27	4.8	2.1	4.77	26.6
S3RVT	50	198	0.81	0.25	7.1	9.8	5.92	3.55
S4RVT	61	230	0.92	0.21	4.6	5.1	5.29	2.27

CC = correlation coefficient; Channel = the number of unipolar channels; LE_E = localization error of the earliest site; LE_L = localization error of the latest site; Needle = the number of plunge-needle electrodes; RE = relative error; RVT = reentrant ventricular tachycardia; t = the time length of analyzed reentrant ventricular tachycardia in body surface potentials; ω_0 = the main oscillating frequency of reentrant ventricular tachycardia.

The intracardiac mapping results of S2RVT1 are presented in Fig. 6. The reentrant VT beat analyzed is framed in a red rectangle on the top left corner. The two reentry loops that composed a figure 8 reentry circuit are depicted in the left middle row with the unipolar electrogram of each channel presented on the right. The activation time is defined as the time with the maximum negative first derivative, which is marked by a red vertical line, and the exact time is on top of it with a unit of millisecond. Loop A to B to G forms an anterior top loop that passes through the left ventricle, the septum and the right ventricle. Loop A to H to G forms another lateral loop that circulates in the right ventricle. The conduction block is denoted by a black rectangle between site A and site G. The bottom left row demonstrates the 3D colormap of the intracardiac activation time with red representing the earliest activated region and blue the latest activated region. Here the anterior loop is denoted by two black dashed lines and the lateral loop is shown in the orange dashed lines. The cross section view of this color map is on the right with one sagittal view on the bottom left corner. The view of the anterior loop is the same as that of the 3D color map.

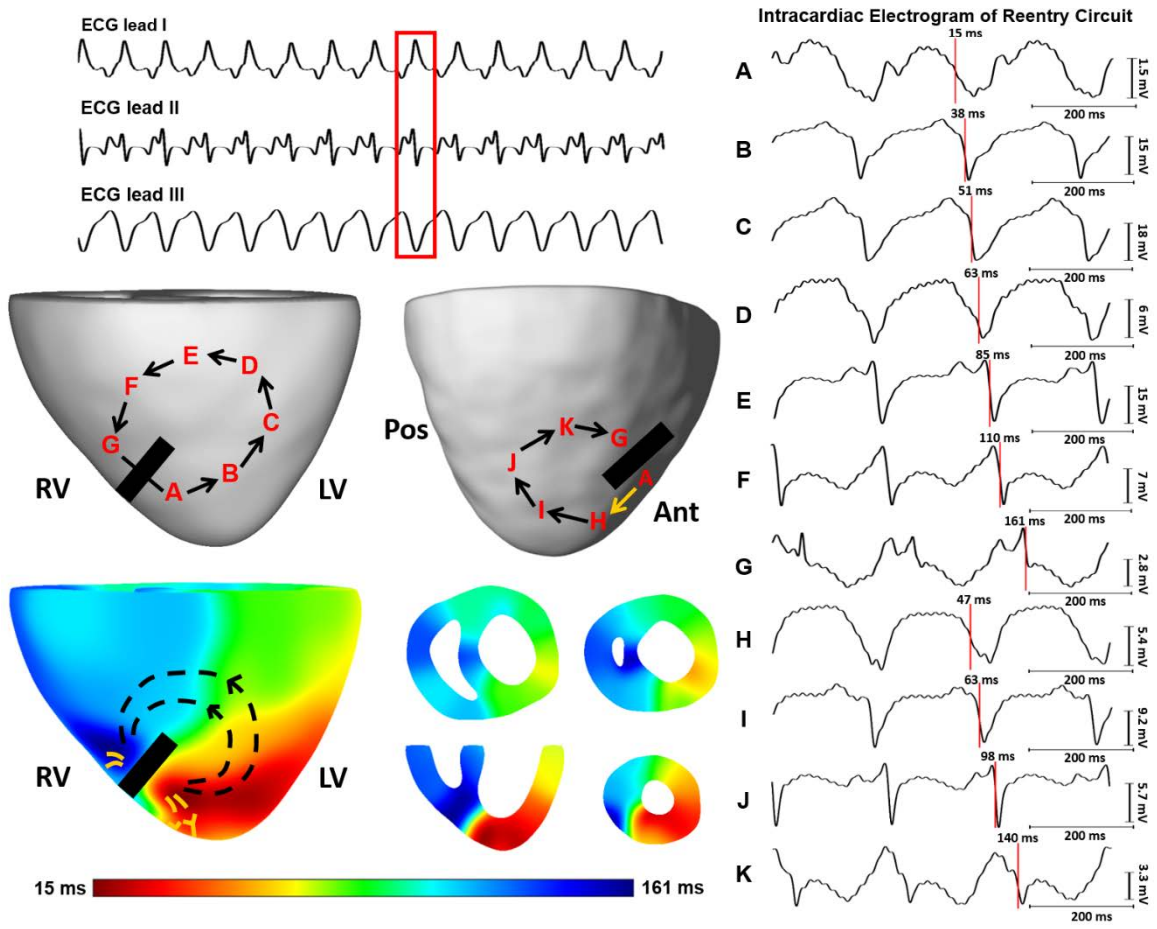

Figure 6 Intracardiac mapping results of S2RVT1. The analyzed reentrant ventricular tachycardia beat is framed in a red rectangle on the top left corner. Two loops that compose the figure 8 reentry circuit are depicted in the middle left row. The corresponding activation time map is shown in the bottom left row. Its cross section and sagittal view are listed on the right of the activation time map. The individual unipolar electrogram of each site in the circuit with activation time marked on top is demonstrated on the right column. Ant = anterior view of the heart, LV = left ventricle, Pos = posterior view of the heart, RV = right ventricle.

Figure 7 provides plots of ECG Lead II used for the analysis and the power spectrums of four reentrant VTs. The power spectrums were used to determine the main oscillating frequency. The last column is the Signal-to-Noise Ratio (SNR) determined from the power spectrum. Signal refers to the power amplitude of the main oscillating frequency, namely the maximum power amplitude in the plot. It is marked with a red star in the figure. Moreover, the noise is the largest amplitude of power except the main frequency and its

harmonics (a wave with a frequency that is a positive integer multiple of the main frequency) which is pointed by a black arrow in the figure.

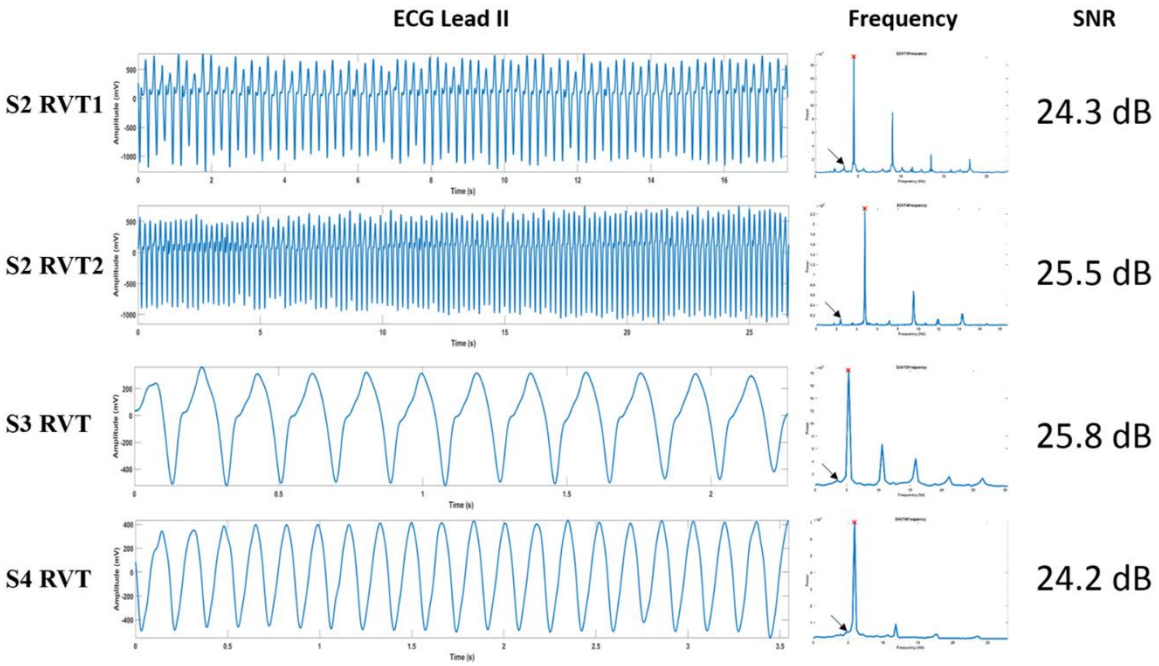

Figure 7 ECG Lead II and power spectrum of four reentrant VT in the swine. **First column:** ECG Lead II plots of analyzed time segments. **Second column:** Power spectrum of body surface potentials after bandpass filtering and PCA filtering. **Third column:** Signal-to-Noise Ratio (SNR) determined from the power spectrum.

Figure 8 illustrates the imaging results of the four reentrant VTs. Each panel represents one reentrant VT. Within each panel, the measured 3D intracardiac activation time maps are listed in the first row. The corresponding imaged activation sequences are presented in the second row. They are color-coded from the red to the blue. The yellow star denotes the earliest activated site and the orange star denotes the latest activated site. For the third row, the red infarction area is plotted in a translucent way inside the ventricular myocardium and the infarction extent was estimated from the delay-enhanced MRI images of the heart. 3D views in these three rows share the identical lightening and view. Cross section views of the measured and infarction are the same. Since there is a discrepancy between the measured and the imaged, the cross section views of the imaged are chosen to show the earliest and the latest activated sites. The reentry pathways of three out of four reentrant VTs were formed in the anterior border and one was in the posterior

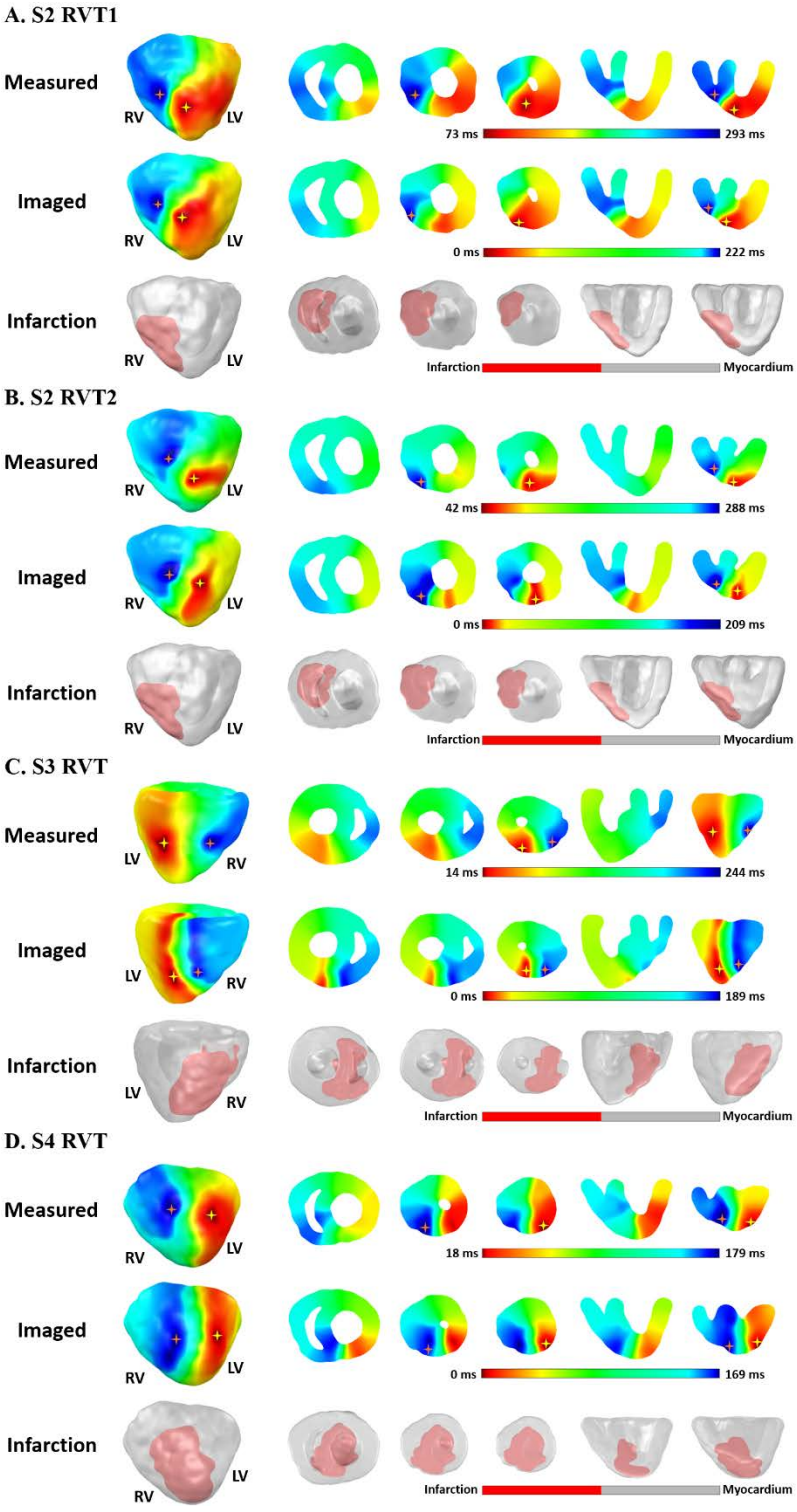

border. Plunge-needle electrodes were more densely placed in the anterior side, and there were fewer electrodes in the posterior. This explains why in Swine 3 the distance between the earliest and latest activation site in imaging results was longer than that in the measured results. In the other three reentrant VTs, the distances were similar between the imaged and measured results.

Figure 8 Imaging results of four reentrant VT in the swine. The first and the second columns are the measured intracardiac activation time maps and the reconstructed activation time maps. Activation time maps are color coded from red to blue with red indicating the earliest activated site and blue the latest. Yellow stars are used to mark the earliest site and orange stars stand for the latest site. The infarction extent of each pig is in the third column and the red object is the infarction. Frequency analysis of reentrant ventricular tachycardia is shown in the fourth column. LV = left ventricle, RV = right ventricle, RVT = reentrant ventricular tachycardia.

3.4 Discussion

3.4.1 Property of SSF

To our knowledge, SSF is the first imaging algorithm designed for imaging periodic ventricular arrhythmias especially for imaging the 3D reentrant circuit in reentrant VT. The inverse problem formulates in the frequency domain and solely utilizes the main oscillating frequency components, which results in the robust performance of SSF against noise and its less computational time. The constraint is formed on the basis of spatial gradient sparse which was not taken into consideration in the previous cardiac electric imaging algorithms and this leads to a higher spatial similarity between imaged activation time maps and simulated (or measured) activation time maps.

SSF is built on a tetrahedron model transformed from the conventional rotating dipole model. In the time domain, the time segment of a reentrant beat used for analysis is hard to decide since this is a reoccurring event within the whole ventricle. The starting time point of a beat in the butterfly plot of body surface potentials is not associated closely with the starting point of a reentrant circuit. This makes it difficult to image the activation sequence of a reentry circuit using an imaging algorithm developed in the time domain. However, in the frequency domain, the activation sequence is encoded into the phase. To express the phase of a cardiac source, a tetrahedron model with edges serving as the new cardiac sources can clearly define the amplitude and phase of the current density that cannot be done in a rotating dipole model.

The tetrahedron model and spatial gradient sparse in the frequency domain consist of the novelty that SSF possesses. The statistics in the focal VT simulation have shown the robustness of SSF against noise and a better spatial balance than WMN when imaging deep sources. The statistics in the reentrant VT swine study demonstrated that SSF was able to reconstruct the global reentry circuit with a good accuracy. Regardless of a long train of focal VT beats or reentrant VT beats, SSF could reconstruct the activation sequence with one shot.

3.4.2 Application to Reentrant Ventricular Tachycardia

In a series of studies on reentrant ventricular arrhythmias in the late myocardial infarction period in dogs [67]–[72], researchers have investigated this type of reentrant VTs

from a variety of aspects, such as epicardial mapping of reentrant VTs, electrophysiologic-anatomic correlation of reentrant circuits, spontaneous versus induced reentry, correlation of activation and refractory maps and entrainment and termination of reentrant VT. Infarction in these dogs was created by a ligation on the LAD artery, and experiments were done 3-5 days after the ligation. It has been shown that regardless of the anatomical localization of reentrant circuits (epicardial, intramural, or subendocardial), their dimension or mechanism of initiation (spontaneous or programmed premature stimulation), reentrant excitation always occurred in a figure 8 configuration. [69]

We tested the proposed method on a swine model in which the infarction was created by a LAD artery occlusion and the experiments were done 2 months after the occlusion. Based on the location of the infarction and the time length of infarction existence, our study results shared many similarities with those obtained from the canine model. We observed a figure 8 configuration of reentrant circuits in the swine model both from the 3D intracardiac mapping results (Fig. 6) and from the 3D imaging results (Fig. 8). The infarction zone were made of cells that showed a wide variety in degrees of partial depolarization, reduced action potential amplitude and decreased upstroke velocity [68], and from the intracardiac electrograms in Fig.6, we could see that the reentrant circuit was consisted of myocardial regions with a wide range of action potential amplitudes (from 2 mV to 25 mV). The reentrant circuit we obtained is a macroreentry, and the possible reason of it could be the existence of a tract of surviving tissue that traverses the infarct. [73]

Inside the myocardial infarction area, surviving muscle fibers and strands of fibrous tissue were interwoven which was supported by the study in patients. [74] The reentry occurred at the border of the infarct and the larger subendocardial muscle mass. [75] This concept was further supported by comparing locations of conduction block with the infarction extent in the ventricles in Fig. 8. Since the intracardiac-mapping results and infarction results shared exactly the same cross section view, the earliest and latest activated site in the reentrant circuit located on the border of the infarct and the normal tissue.

3.4.3 Clinical Implication

To terminate the reentrant VT via ablation, information such as the central common pathway, VT exit site and lines of conduction block is needed. Effort has been made to directly map the reentrant circuit by endocardial mapping [73], epicardial mapping [67], [68] or entrainment mapping. [76] However, they were limited by the region that was covered and were unable to capture the macroreentry throughout the ventricles simultaneously. They were also invasive procedures that may put patients under prolonged procedure time. Recently, a noninvasive epicardial imaging technique was applied to infarcted canine hearts lying inside a human torso model [77]–[79]. Although it was able to reconstruct the reentry pathway and its key components based on the imaged epicardial potential, the initiation of a reentry beat was detectable only when it reached the epicardium that was expressed as a breakthrough on the epicardial potential map. We reconstructed the reentrant circuit throughout the myocardium in situ and compared the results with those from simultaneous intracardiac mapping. We have successfully recorded 4 reentrant VTs in pigs, and achieved an average CC of 0.88±0.05, an average RE of 0.23±0.03, an average LE of earliest activated sites of 6.3±1.9 mm, and an average LE of latest activated sites of 6.3±3.4 mm. RF ablation at the exit, central and proximal sites in the reentry circuit results in a high incidence of termination. [76] The pathway of reentrant VT, VT exit site and lines of conduction block of a reentrant VT are clearly shown in the 3D imaged activation sequence maps, which would reduce the searching area for ablation and the ablation time, and finally help in the successful termination of reentrant VT.

3.4.4 Study Limitation

Our study is limited by the number of reentrant VTs obtained from four pigs. However, compared with the induced rate in dogs [68], we have achieved a 75% induced rate in pigs. All the reentrant VTs were induced in swine hearts with myocardial infarction produced by LAD occlusion. In clinical, myocardial infarction could occur in other regions and reentrant VTs could happen in a normal heart. The performance of SSF needs to be evaluated in more diverse animal models in the future. The spatial resolution of measured activation sequences is limited by the number of plunge-needle electrodes in the myocardium. The positions of plunge-needle electrodes were digitized in vitro. Within all these limitations, we have shown that SSF was able to reconstruct activation sequences of

a reentrant VT noninvasively and we have successfully depict the reentry circuit in the swine hearts.

Chapter 4

Activation Recovery Interval Imaging

4.1 Introduction

Dispersion of ventricular repolarization due to abnormal activation contributes to the susceptibility to cardiac arrhythmias [80]. Studies have shown the relationship between inhomogeneity of ventricular repolarization and enhanced ventricular arrhythmia vulnerability [81]–[86]. Refractory period, transmembrane action potential duration, and activation recovery interval (ARI) have been used to understand the properties of ventricular repolarization. Compared to the other two measurements, ARI has the advantage of being able to be extracted from multiple, simultaneously recorded electrograms and reflecting the dynamics and spatial characteristics of repolarization.

A method was first reported by Wyatt *et al* [87], [88] to estimate activation and repolarization times from unipolar electrograms. By comparing the difference between the repolarization time and the activation time with simultaneously recorded in vivo transmembrane action potential durations, Wyatt method was shown to be a good estimation of action potential durations (APDs). Later, ARI was clearly defined as the interval between times of activation and repolarization, and was used in two animal studies, which demonstrated high correlation between ARI from unipolar electrograms and refractory periods or action potential durations under a variety of conditions. [89], [90] In Wyatt method, activation and repolarization time are defined as the time of minimum derivative of the QRS and the time of maximum derivative of the T wave in unipolar electrograms respectively.

T wave polarities correspond to different repolarized regions, and there has been a controversy over the determination of repolarization time for positive T waves in unipolar electrograms. Chen *et al* [91] proposed an alternative method in which the minimum derivative on the downslope of the positive T waves was chosen to represent the local repolarization. This study and other following studies [92], [93] have observed a better correlation between ARI and MAP 90% (90% repolarization of monophasic action

potential recordings). However, the alternative method lacks theoretical foundation. To justify the use of Wyatt method, Coronel et al [94] have presented experimental evidences and Potse et al [95] have validated through a simple theoretical model that the maximum derivative of T waves should always be used regardless of T wave polarities. Finally, a more recent study [96] identified the sources of measurement bias of Wyatt method and supported previous assertions that alternative method does not reliably represent either repolarization time or MAP 90%. So the determination method of repolarization time in unipolar electrograms from CARTO system to evaluate the performance of ARI imaging in this study is Wyatt method.

Besides validating the use of ARI from invasive recordings, researchers have always wanted to discover parameters that could reflect repolarization properties from noninvasive recordings. It has been shown that indices derived from 12-lead ECG are inadequate [97], [98] and even high-resolution body surface potential map (BSPM) has its limit in identifying local changes in repolarization. [99] In this case, cardiac imaging technique comes as a better choice in the sense of being noninvasive and timesaving and providing detailed cardiac activities. Epicardial potential imaging such as noninvasive electrocardiographic imaging (ECGI) was developed [18] to reconstruct epicardial potentials from BSPMs and has been applied to a variety of conditions. [100] However, since ventricular repolarization is inhomogeneous [101] and one can only infer deep source activities from epicardial potential maps, a 3D cardiac imaging technique could provide more direct information such as activation time and repolarization time in 3D space and would be considered more desirable.

Our group has developed a 3D cardiac electrical imaging (3DCEI) technique [26], [49] to estimate the equivalent current density at each cardiac source location from BSPMs and derive activation time from the time course of current density. This method has been quantitatively evaluated in animal models under different conditions such as pacing, ventricular tachycardia, drug-induced QT prolongation and nonischemic heart failure. [37], [43], [47], [102] Recently, we applied 3DCEI to atrial arrhythmias by extracting frequency features from the reconstructed current density. [50]

Studies have shown that ventricular repolarization potential distributions during ectopic beats were influenced by transventricular gradients (gradients from one side of the heart to the other) [103] and the longest ARIs were located at the sites of earliest activation and shortest at the latest activation areas during pacing. [92] In this study, we extended the application of 3DCEI to repolarization properties by reconstructing ARI distributions from the time course of current density and investigated the role of ARI in guiding ablation procedure in PVC patients.

4.2 Methods

4.2.1 Patients

BSPMs were recorded in 10 PVC patients (Male= 4, Female= 6, average age= 47.8 ± 11.7 years old) before the EP procedure with spontaneous PVCs detected. None of them has undergone ablation procedure before. Patient characteristics and selective medical records are summarized in Table 4. Study protocols were approved by the Institutional Review Board of University of Minnesota and Shanghai Ruijin Hospital (affiliated with Shanghai Jiao Tong University School of Medicine, Shanghai, China). All patients signed written consent forms before this study.

Table 4 Patient Statistics of ARI Imaging Study

Patient	Age	Gender	Heart Rate (bpm)	Blood Pressure (mmHg)	Antiarrhythmic Medication	Medical History	PVCs/24 h
1	41	F	74	116/77	None	Diabetes	15160
2	53	M	70	105/63	Bisoprolol	Allergic to penicillin	25630
3	43	M	75	121/64	Amiodarone	Hypertentsion	N/A
4	71	F	70	117/61	Aspirin, Lipitor	Atherosclerosis of coronary artery and carotid artery, cervical disc herniation	21100
5	54	F	80	118/67	Moracizine	Allergic to cephalosporin	13441
6	37	M	95	137/86	None	Sublingual gland excision	27161 / 23 h
7	42	F	78	115/75	None	None	26337
8	43	M	82	150/80	None	None	39476
9	33	F	84	100/55	None	Cardiac arrhythmias, asthma	51226
10	61	F	82	129/79	Amiodarone, Moracizine, metoprolol	Paroxysmal palpitation	8470

bpm = beats per minute, F = female, M = male.

4.2.2 Experimental Design

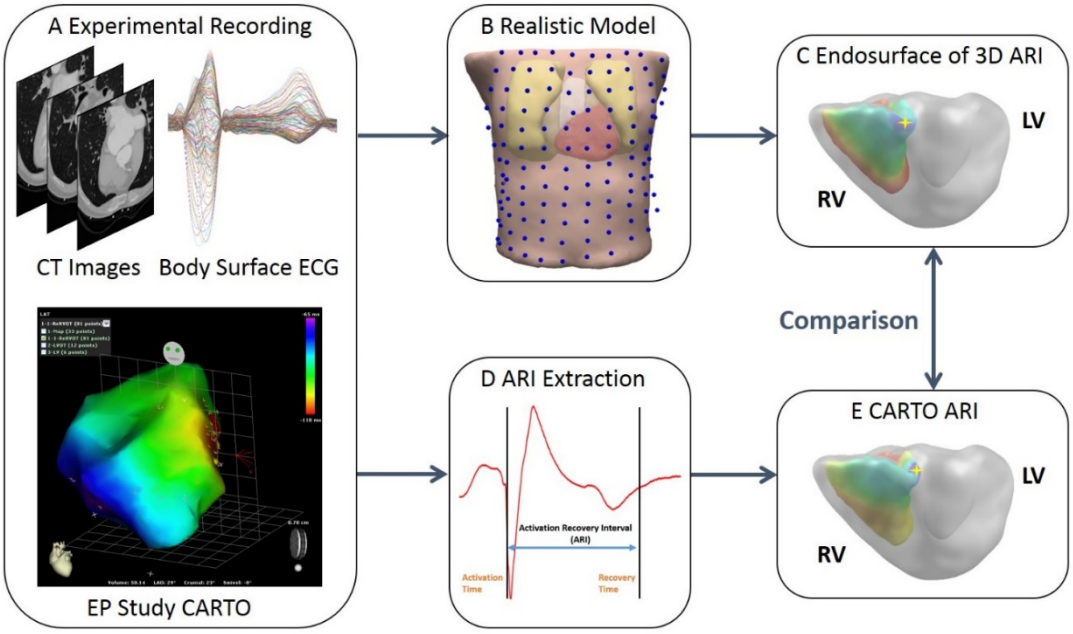

Figure 9 Schematic diagram of ARI imaging and validation in PVC patients. A: Experimental recordings include cross-sectional CT slices showing detailed heart geometry and torso boundaries, butterfly plot of multiple-channel ECGs and local activation time maps recorded during EP study. B: Realistic heart-torso model (blue dots showing body surface electrodes). C: Endocardial surface of ARI maps by applying ARI imaging. D: ARI extraction of individual recording sites from unipolar electrograms. E: Interpolated endocardial surface of ARI maps from CARTO system. 3D = 3-dimensional, ARI = activation recovery interval, CT = computed tomographic, ECG = electrocardiogram, EP = electrophysiology, LV = left ventricle, PVC = premature ventricular contraction, RV = right ventricle.

Schematic diagram of the study is shown in Fig. 9. CT images were collected before EP study. A continuous volume scanning from the level of great vessel to the diaphragm was performed to obtain the heart geometry with a slice thickness of 0.4 mm. And another scan from the collar bone level to lower abdomen with a slice thickness of 6 mm was to get a complete torso geometry. These two sets of CT images were registered based on important cardiac anatomical landmarks. A realistic model including torso, lungs, epicardium, and ventricles was built from CT images by using a commercial software (Curry 6.0, Neuroscan, North Carolina, USA) for segmentation and registration.

Two hundred and eight Ag-AgCl carbon electrodes were placed on the front (n=140) and back (n=64) of patients when they were in Fowler's position. The electrodes were digitized by using an electromagnetic digitizer (Fastrak, Polhemus Inc., Colchester, VT, USA). The electrodes were then connected to BioSemi ActiveTwo system (BioSemi, Amsterdam, Netherlands) with a sampling frequency of 2k Hz to record body surface ECGs. Recording lengths were summarized in Table 1 for each patient. Patients were asked to keep still with slow respiration to reduce motion artifacts during recording.

After each EP study, we collected CARTO files that include endocardial surface of either or both ventricles, endocardial local activation time maps, ablation sites and unipolar electrograms. The endocardial surface of ventricles was registered with the segmented heart from CT images.

After registering body surface electrodes with the realistic model (Curry 6.0), a boundary element model (BEM) was built and by implementing ARI imaging technique, a 3D ARI map was reconstructed. On the other hand, ARI was extracted from unipolar electrograms and was interpolated to get a CARTO ARI map. 3D ARI map was compared with the CARTO ARI map quantitatively. Detailed descriptions of ARI imaging technique and ARI extraction from unipolar electrograms are stated in the following sections.

4.2.3 Imaging Principle of ARI Imaging

Follows the forward modeling in the time domain (Eq. (2.3)), $\emptyset_b(t)$ is a $M\times1$ vector of body surface potentials at M electrode positions at time t and $J(t)$ is a $3N\times1$ vector of the equivalent current density at N source locations at time t. Since $3N$ is usually much larger than M, finding $J(t)$ given $\emptyset_b(t)$ is an ill-posed inverse problem that requests mathematical regularization. A generalized Tikhonov regularization is applied to solve this inverse problem:

$$\min_{J(t)} \left(\|\emptyset_b(t) - LJ(t)\|_2^2 + \lambda\|WJ(t)\|_2^2\right) \qquad (4.1)$$

where W is the depth weighting matrix calculated from L and λ is the regularization parameter determined by L-curve method.

After solving the inverse problem on QRS complexes and T waves separately, the time course of the equivalent current density at each source location is obtained. According to the maximum criteria [26], the activation time τ_a(or repolarization time τ_r) is when the amplitude of $J(t)$ reaches its maximum during the duration time T at a fixed location p :

$$\tau(p) = \max_{t \in T}\big(J(p,t)\big) \qquad (4.2)$$

Activation recovery interval (ARI) is defined as the interval between repolarization and activation, so ARI at location p is:

$$ARI(p) = \tau_r(p) - \tau_a(p) \qquad (4.3)$$

4.2.4 ARI Extraction from Unipolar Electrograms

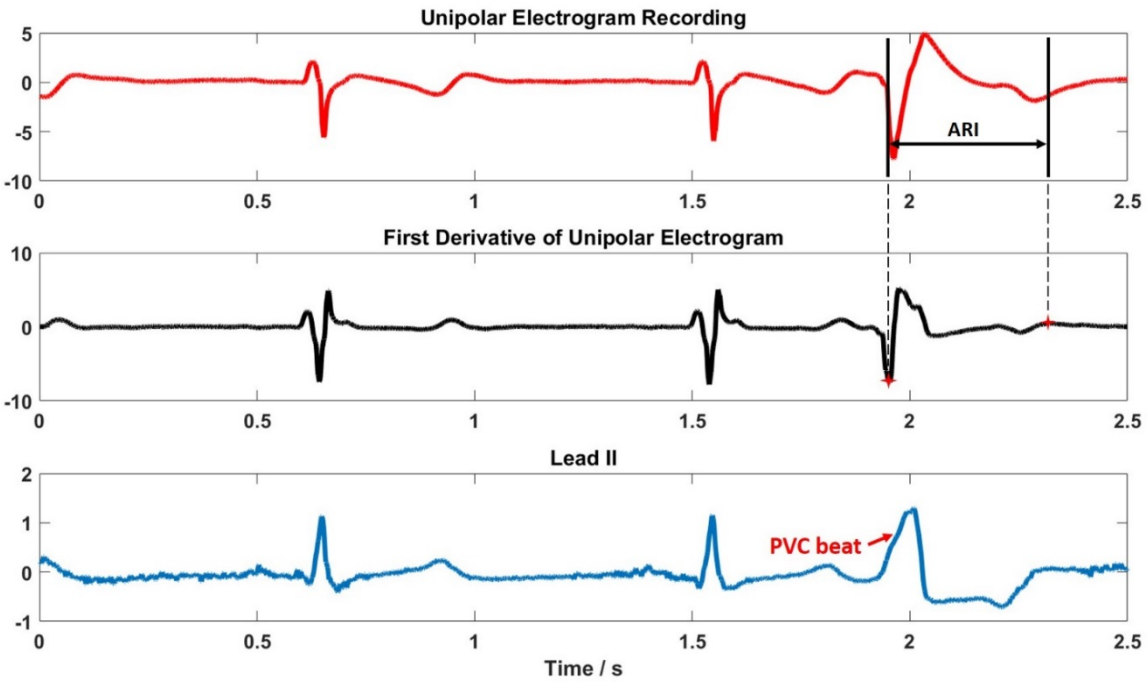

Figure 10 ARI extraction from unipolar electrograms. Top: Unipolar electrogram of a recording site. Middle: First derivative of unipolar electrogram to aid in determining the activation time (minimum derivative) and repolarization time (maximum derivative). Red stars represent these two time points. Bottom: Simultaneous recording of Lead II on the body surface to identify a PVC beat. Amplitude unit of recordings is mV, and time unit is second. ARI = activation recovery interval, PVC = premature ventricular contraction.

Unipolar electrograms were included in CARTO files. At each recording site, a 2.5-second unipolar electrogram was recorded with corresponding 12-lead ECGs simultaneously. The unipolar electrogram and the first derivative of the unipolar electrogram were plotted along with Lead II from 12-lead ECGs to help identify PVC beats in Fig. 10. The minimum derivative in QRS and the maximum derivative in T wave were automatically detected and marked as activation time and repolarization time respectively. Finally, ARIs at recording sites were interpolated to endocardial surface to get an endocardial ARI map.

4.2.5 Statistical Analysis

To evaluate the performance of ARI imaging, a quantitative comparison was made between two endocardial ARI maps: one was extracted from the 3D ARI map and the other was interpolated CARTO ARI map. For patient 1, 2 and 4, unipolar recording sites spread throughout the whole chamber of either left ventricle or right ventricle, which enables us to directly extract the endocardial surface from 3D ARI map and also interpolate ARIs to the same endocardial surface. However, for the other 7 patients, because of the small number of unipolar recording sites and the accompanying small region of CARTO endocardial map, 3D ARI map was projected to and ARIs were interpolated to the same CARTO endocardial surface for comparison. Statistics include correlation coefficient (CC) and relative error (RE) between two endocardial ARI maps, localization error between the longest ARI sites (centers of mass with longest ARIs) in two maps (LE-map), and also LE between the longest ARI site in 3D ARI map and the ablation sites (LE-ablation).

4.3 Results

In total, 100 PVC beats (10 for each patient) were analyzed. A good correlation was found with an overall CC of 0.86±0.05 and a RE of 0.06±0.03. The average LE-map is 4.5±2.3 mm and the average LE-ablation is 4.0±1.3 mm. Since the longest sites in both ARI maps are at a different area as ablation sites in patient 2, LE-ablation data of patient 2 was not taken into account when calculating the average LE-ablation. Based on the activation time maps of activation imaging results, PVC originated from right ventricular outflow tract (RVOT) in 9 out of 10 patients, 7 in the right ventricle free wall side and 2 in the septum side. One patient (patient 2) who was diagnosed as having right bundle branch

block (RBBB) had the ectopic beats initiated from left anterior fascicle in the left ventricle. These are in accordance with the clinical ablation outcomes. From 3D ARI maps of ARI imaging results, the site with the longest ARI was at the same location as the clinical ablation outcome, with only one exception that for the patient with RBBB, the longest ARI site lied in left posterior fascicle in the left ventricle. These were summarized in Table 5 along with BSPM indices and statistics of 10 PVC beats for each patient.

Table 5 Statistics of Ablation Outcome and Data Analysis

Patient	Diagnosis	Ablation Outcome	Recorded Longest ARI site	Imaged Longest ARI site	BSPM Recorded (minutes)	QRS (ms)	T-wave (ms)	PVC beat (ms)	BSPM ARI (ms)	Unipolar Recording Sites (No.)	CC	RE	LE-map (mm)	LE-ablation (mm)
1	PVC	RVOT free wall	RVOT free wall	RVOT free wall	10	101	131	362	130	41	0.83±0.01	0.03±0.01	4.1±0.6	4.1±0.9
2	PVC, RBBB	Left *Anterior* Fascicle	Left *Posterior* Fascicle	Left *Posterior* Fascicle	24	88	166	379	125	34	0.86±0.04	0.05±0.01	7.7±2.0	N/A
3	PVC, Nonsustained VT	RVOT free wall	RVOT free wall	RVOT free wall	12	113	171	362	78	13	0.84±0.02	0.04±0.02	3.4±2.3	4.1±2.5
4	PVC, Nonsustained AT	RVOT free wall	RVOT free wall	RVOT free wall	14	113	167	416	136	40	0.81±0.02	0.08±0.02	3.4±1.1	5.0±0.5
5	PVC	RVOT free wall	RVOT free wall	RVOT free wall	21	119	162	387	106	18	0.85±0.01	0.11±0.01	2.6±0.1	3.7±0.2
6	PVC, Nonsustained VT	RVOT free wall	RVOT free wall	RVOT free wall	13	126	179	394	89	52	0.84±0.01	0.08±0.01	5.9±1.0	4.8±0.8
7	PVC	RVOT free wall	RVOT free wall	RVOT free wall	14	111	156	411	144	82	0.94±0.01	0.06±0.01	3.6±0.3	3.2±1.0
8	PVC	RVOT septum	RVOT septum	RVOT septum	21	113	155	326	58	23	0.91±0.04	0.05±0.01	5.1±1.7	3.1±1.1
9	PVC	RVOT free wall	RVOT free wall	RVOT free wall	24	92	154	356	110	11	0.81±0.06	0.01±0.01	1.3±0.1	4.8±0.7
10	PVC	RVOT septum	RVOT septum	RVOT septum	17	97	169	350	84	22	0.86±0.03	0.06±0.04	7.1±2.0	3.5±1.3
Average	N/A	N/A	N/A	N/A	17	107	161	374	106	34	0.86±0.05	0.06±0.03	4.5±2.3	4.0±1.3

AT = atrial tachycardia, ARI = activation recovery interval, BSPM = body surface potential maps, CC = correlation coefficient, LE-ablation = localization error between the longest ARI sites in imaging ARI map and the ablation sites, LE-map = localization error between the longest ARI sites in imaging ARI map and CARTO ARI map, PVC = premature ventricular contraction, RBBB = right bundle branch block, RE = relative error, RVOT = right ventricular outflow tract, VT = ventricular tachycardia.

Figure 11 shows the results for three patients (Patient 1, 2 and 4) with recording sites covering the full chamber. The first column are the imaged activation time maps, in which white stars represent the earliest activated sites. The second column refers to the imaged endocardial ARI maps and the fourth column the interpolated CARTO ARI maps. In both columns, the longest ARI sites are labeled by yellow stars. In between, there are three cross section views of imaged 3D ARI maps. All the maps are colored from red to blue, with red representing the minimum and blue the maximum. The time scales of imaging ARI maps are from both ventricles and the time scales of CARTO ARI maps are determined by the ARI values of recorded sites. The PVC beats analyzed were marked in

Lead II electrograms. The time segment between red vertical lines was used for activation imaging and the time segment between magenta vertical lines was the input for repolarization imaging. In patients 1 and 4, the earliest site in activation and the longest ARI sites in both ARI maps are in the same region, namely RVOT right ventricle free wall side. For patient 2, activation started at left anterior fascicle while the longest ARI site located at left posterior fascicle. The CC and LE-map are shown underneath.

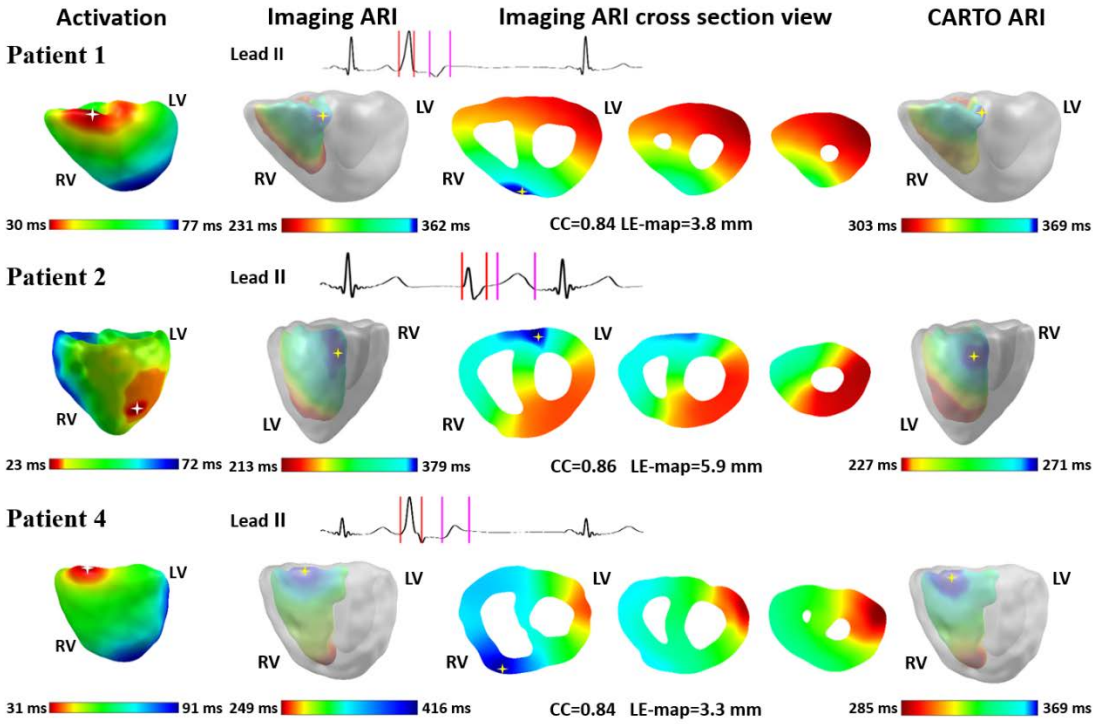

Figure 11 ARI results with recording sites covering a full chamber of ventricles. First column: Imaged activation time maps with white stars representing the earliest activated sites. Second column: Endocardial surface of 3D ARI maps which were obtained by applying ARI imaging to QRS complexes (red vertical lines) and T waves (magenta vertical lines) separately. Third column: Three cross-section views of 3D ARI maps. Fourth column: Interpolated CARTO ARI maps. Yellow stars in the ARI maps represent the longest ARI sites. All the maps were color-coded from red to blue with red denoting the earliest activated or the shortest ARI site and blue stands for the latest activated or the longest ARI site. The time scales of imaging ARI maps are from both ventricles and the time scales of CARTO ARI maps are determined by the ARI values of recorded sites. 3D = 3-dimensional, ARI = activation recovery interval, CC = correlation coefficient, LE = localization error, LV = left ventricle, RV = right ventricle.

Among the other 7 patients with small CARTO-recorded endocardial surfaces, 5 have the PVC beats starting from RVOT right ventricle free wall side and 2 are from RVOT septum side. Representative results of two patients are shown in Figure 12. Because of the small recording area, imaged ARI maps were projected to CARTO-recorded endocardial surfaces and then were compared with interpolated ARI maps quantitatively. The figure format is the same as that in Figure 11.

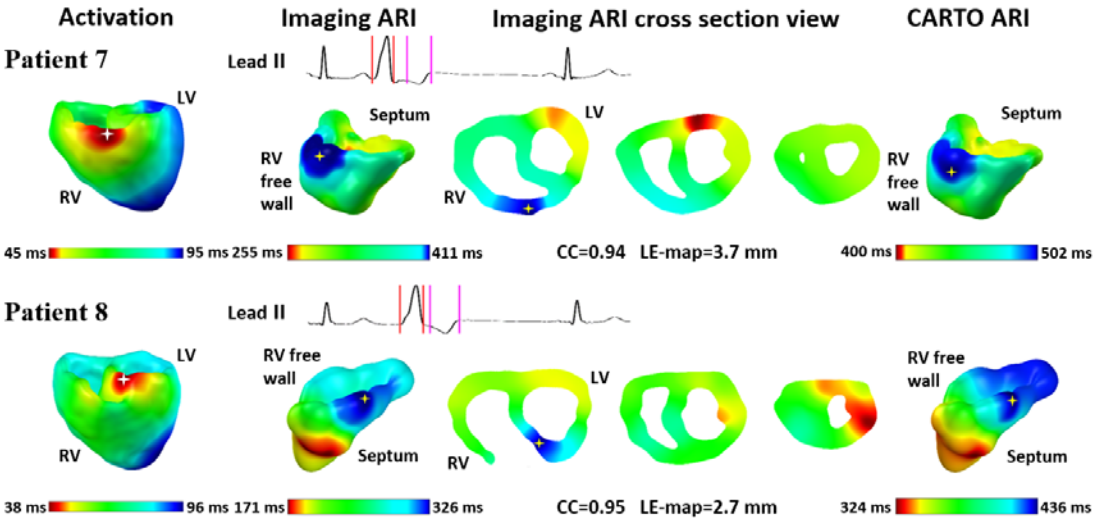

Figure 12 ARI results with fewer recording sites covering regional ventricles. The format is the same as in Fig. 11. The time scales of imaging ARI maps are from both ventricles and the time scales of CARTO ARI maps are determined by the ARI values of recorded sites. 3D = 3-dimensional, ARI = activation recovery interval, CC = correlation coefficient, LE = localization error, LV = left ventricle, RV = right ventricle.

4.4 Discussion

This study used 3D ARI imaging technique to determine the spatial pattern of activation and repolarization and to construct ARI maps in PVC patients noninvasively. Quantitative comparisons were made between imaging results and clinical recordings.

4.4.1 3D ARI Imaging

Previous to this study, ventricular repolarization patterns could only be reflected from epicardial potentials [104] noninvasively or from endocardial potentials [105] invasively. Although activation pattern may remain unchanged, repolarization could vary

and thus plays an important role in the susceptibility to cardiac arrhythmias. Given the inhomogeneous and dynamic nature of repolarization pattern, a 3D ARI imaging technique is essential. We have shown the capability and performance of 3DCEI by imaging activation patterns under various conditions in the past. This study expanded our study scope to repolarization in humans.

4.4.2 Quantitative Comparison and Localization of the Longest ARI Site

In the previous noninvasive imaging studies, repolarization patterns were shown and discussed. However, a quantitative measurement was lacked. In the current study, we evaluated the performance of 3D ARI imaging by comparing the imaging results with ARI maps extracted from clinical unipolar electrograms quantitatively. The time length of the imaged ARI in Fig.11 and Fig. 12 was in concordance with the ARI time length estimated from BSPM in Table 5. In addition, the time length derived from the unipolar electrograms was found to be longer than the imaged ones. This could be explained by the direct contact of unipolar electrodes deprived of the smearing effect due to electrical propagation through a volume conductor. Thus, imaged ARIs were shorter than CARTO ARIs. Besides the three patients with recorded sites covering a full chamber, the other seven patients were mapped in a small region around the target ablation sites. Therefore, the recorded ARIs were much longer than those of both ventricles.

4.4.3 Clinical Implication

During ectopic activity such as in PVC or pacing, repolarization time is mainly determined by the activation sequence since activation time differences are much larger than local repolarization (action potential duration). This is supported by previous findings in which activation time was inversely correlated with ARI during premature stimulation in patients with normal ventricles. [105], [106] Our results are in accordance with the theory and previous findings in the aspect of detecting the longest ARI sites are close to the origins of PVCs in 9 PVC patients with normal ventricles.

Discrepancy occurred in patient 2 who had RBBB in the ventricles. Normally, activation is conducted through both bundle branches of the conduction system. However, during RBBB, with the right bundle branch blocked, the right ventricle is activated by the impulses travelled through myocardium from the left ventricle instead of being activated

through the bundle of His-Purkinje fibers and the left ventricle is still normally activated by the left bundle branch. Anatomically, the left bundle branch divides into the left anterior fascicles and the left posterior fascicles. From the activation time map and the recorded successful ablation site's location, PVCs were initiated by the left anterior fascicles in patient 2. What is interesting is that the longest ARI site was in the left posterior fascicles in clinical ARI map and imaging ARI map. Whether this site would be the future potential origin of PVCs remains unclear and requires a follow-up observation. For now, 3D ARI imaging has been reflecting repolarization changes faithfully in ectopic activities.

4.4.4 Study Limitation

The patient population (n=10) is small and the diversity of patients is limited since most patients have origins of PVCs at RVOT. Not all the patients were mapped within the full chamber, which may contribute to the higher correlation coefficients in some patients because of the projection and interpolation over a relatively small area. Within these limitations, 3D ARI imaging provides an insight into the global pattern of repolarization and the capability of ARI in ectopic activities.

Chapter 5

Localization of Origins of Premature Ventricular Contraction

5.1 Introduction

Since its invention, the 12-lead ECG has been widely used as a diagnostic test for cardiac arrhythmias and it can be recorded rapidly with portable equipment for a long time by using a Holter monitor. [107] A normal heart beat would produce four entities on the ECG: a P wave, a QRS complex, a T wave and a U wave. They represent different electrophysiological stages of the heart: atrial depolarization, ventricular depolarization, ventricular repolarization and papillary muscle repolarization. Among them, the QRS complex is of the most interest to cardiac electrophysiologists since a majority of ventricular arrhythmias is reflected by the changes of morphology on the QRS complex.

As introduced in Section 2.1 and 2.2, premature ventricular contraction (PVC) is one of the most common ventricular arrhythmias. Pace mapping is one of the predominant mapping techniques being used in clinical settings. [108] If the morphology of QRS complex by pacing at a site matches well with the VT or PVC observed on the 12-lead ECG, this site is considered to be a potential ablation site. Pace mapping is done by stimulating at different endocardial sites, so it is invasive. Non-invasively, researchers have been investigating features of the QRS complex obtained from the 12-lead ECG to help identify ablation targets for PVC and VT. [109]–[111] Some typical characteristics of the QRS complex used for localization are QRS width, QRS axis, QRS patterns (qR, QS, RsR' and so on), R wave amplitude and concordance.

Some characteristics of the QRS complex are easy to calculate automatically; however, for other features that involve a pattern recognition, it is subjective to some degree and requires expertise obtained from a long-time training.

Neural network is well known for recognizing patterns and classification. [112]–[114] The accuracy can be higher than 90% given ample training samples. [115] The input to the neural network can be the original time course of the 12-lead ECG, [116] features extracted from time domain, [117] statistical features, [118], [119] features extracted from

frequency domain, [120] components resulting from different transforms, [121], [122] and outputs from some clustering algorithms. [123] The application of neural network can be the classification among ventricular arrhythmias, [116], [119], [120] classification between normal heart beat and arrhythmias [121], [124], [125] or among all types of arrhythmias. [123] Another important application is the discrimination between healthy subjects and patients, such as patients with myocardial infarction [126]–[128] and patients with coronary artery disease. [122] These applications of neural network are mostly concerned about the state of the heart, whether it is in arrhythmias or have cardiac diseases.

We propose to classify and localize origins of cardiac arrhythmias throughout the ventricles by applying neural networks to 12-lead ECG. The ventricles are divided into 25 segments based on standard myocardial segmentation of the left ventricle [129] and expanded it to the right ventricle. A realistic anisotropic ventricle computer model is used to generate QRS complexes of 12-lead ECG from pacing at all possible ventricular locations. The time course of QRS complexes generated are then fed to convolutional neural network (CNN) for classification and localization purpose.

Epicardial mapping and ablation have expanded considerably in the past few years. It was reported that 13% to 17% VT ablation procedures were epicardial mapping or ablation. [130], [131] On ECG, epicardial VT is reflected as a slow onset of the QRS because the initial part of the wave front progresses slowly until it reaches the Purkinje system at the subendocardium. [132] The intracardiac delay of electrical conduction produces a slurred initial part of the QRS complex (pseudo Δ wave). [133] So the initial part (first half) of the QRS is critical for the detection of an epicardial or endocardial focus. In this study, we use the first half of QRS complexes generated by the ventricle computer model as input to the CNN to classify between an epicardial ectopic beat and an endocardial ectopic beat.

Thus, our proposed method consists of two neural networks: Segment CNN with 25 classifications and Epi-Endo CNN with 2 classifications. The localization of origins of PVC is a function of probability distribution outputs of the two CNNs and the center of gravity of each segments in the ventricular model. Our proposed method was applied to the real 12-lead ECG collected from 9 PVC patients who underwent ablation treatment.

There are other studies to localize the origin of PVC from the 12-lead ECG. Van Dam et al used myocardial activation imaging technique based on an equivalent double layer model to localize the PVC origin, [134]–[136] although positions of 12-lead ECG were unknown, thus the accuracy of results was reduced. In addition, a quantitative measurement of localization error was lacking. In our study, electrodes' positions were digitized and the average localization error was presented by calculating the spatial distance between the CNN predicted sites of origin of PVC and successful ablation sites recorded from EP study in the patient.

Recently, a patient specific model based intracardiac electrograms simulation was done to resemble clinical body surface signals. [137] Our study would be considered a step forward as the model-based noninvasive identification of ablation targets. Materials in this chapter have been previously published. [138]

5.2 Methods

The rationale behind this study is that we assume PVCs are generated by focal sources, and if we train CNN with all the possible 12-lead ECGs resulting from a single-site pacing covering the ventricular volume with a certain level of noise, the CNN will be able to identify which segment the origin of PVC lies in and whether it is an epicardial or endocardial source given a set of 12-lead ECGs. Depending on the probability distribution of CNN output, we could give an estimation of source location based on the classification information.

The realistic anisotropic ventricle model has been introduced in details in Section 2.5. We used this model to simulate ventricular activation process in the heart.

5.2.1 Segmentation of Ventricles and Extraction of Epicardium and Endocardium

In the ventricle current-dipole model that consists of 3,887 cardiac dipoles, the left ventricle was segmented according to AHA standardized myocardial segmentation into 17 segments [129], and the right ventricle was segmented in a similar way as the left ventricle into 8 segments. Thus, the whole ventricle was classified into 25 segments in total. The position and the number of each segment are shown in the middle column of Fig. 13. The

number of cardiac dipoles each segment includes is in the parentheses on the bottom. The left column in Fig. 13 is a visualization of 25 segments. The dipoles lying on epicardium and endocardium were identified and labeled as 1 and 2 respectively, and all other dipoles were assigned 3 as transmural dipoles. Both the left side and the right side of the septum are considered as endocardium.

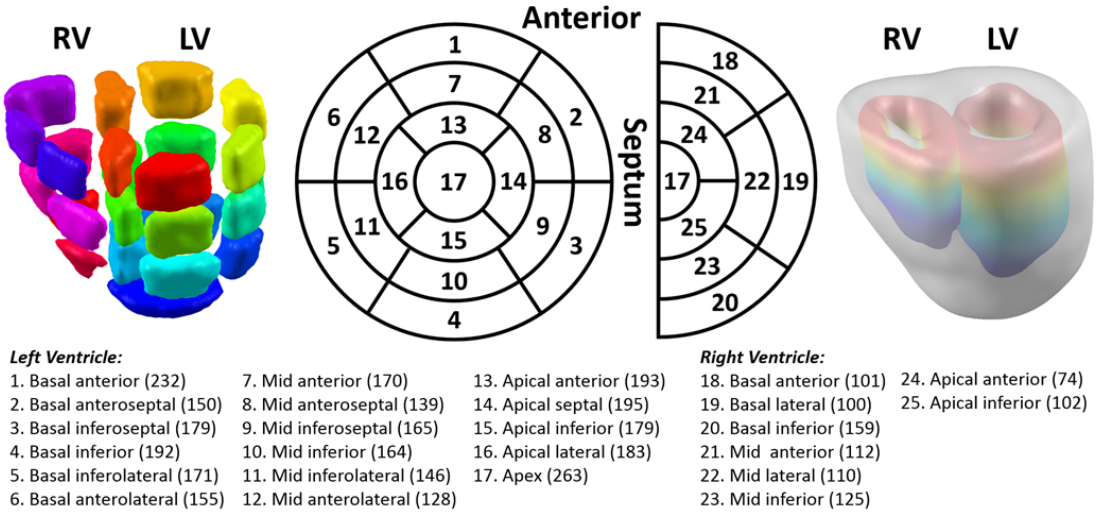

Left Ventricle:

1. Basal anterior (232)
2. Basal anteroseptal (150)
3. Basal inferoseptal (179)
4. Basal inferior (192)
5. Basal inferolateral (171)
6. Basal anterolateral (155)
7. Mid anterior (170)
8. Mid anteroseptal (139)
9. Mid inferoseptal (165)
10. Mid inferior (164)
11. Mid inferolateral (146)
12. Mid anterolateral (128)
13. Apical anterior (193)
14. Apical septal (195)
15. Apical inferior (179)
16. Apical lateral (183)
17. Apex (263)

Right Ventricle:

18. Basal anterior (101)
19. Basal lateral (100)
20. Basal inferior (159)
21. Mid anterior (112)
22. Mid lateral (110)
23. Mid inferior (125)
24. Apical anterior (74)
25. Apical inferior (102)

Figure 13 Segmentation of ventricles. Left ventricle segmentation follows the AHA standardized myocardial segmentation, and the right ventricle is segmented in a similar way developed by the authors. The most right column shows the colorful endo-surfaces of both ventricles and also the gray epicardium. The bottom panel lists all the segments in order, their physical position and the number of cardiac dipoles each segment contains in the ventricle current-dipole model. In total, there are 3,887 current dipoles in the model.

5.2.2 12-lead ECG for Computer Simulation

The torso and lungs were segmented from a high-resolution male torso MRI images (ViP V2.0 IT'IS Foundation, Zürich, Switzerland). Then the boundary element model of heart-torso was built using a commercial software (Curry 6.0, Neuraoscan, North Carolina, USA). 208 body surface electrodes were placed on the front and back of body surface. By multiplying the current-dipoles with the leadfield matrix between each dipole and each electrode, we could get body surface potentials. Among these signals, nine were chosen to generate 12-lead ECG. Three electrodes were selected to represent the electrodes placed on left leg, left arm, and right arm, respectively. So lead I, II III and lead aVL, aVR and

aVF could be derived from the signals of these electrodes. Other six electrodes were selected as V1 to V6 according to their anatomical locations.

5.2.3 Training and Testing of Convolutional Neural Network

Convolutional neural network (CNN) is a type of deep, feed-forward artificial neural network. We used a deep learning toolbox in MATLAB developed by Rasmus Berg Palm [139] to setup, train and test CNN. It uses a sigmoid function as the activation function for feed forward propagation and a gradient descent projection method as the back propagation algorithm. Convolution and pooling were done in 2-dimension (2-D). The stride, namely the number of unit that convolutional kernel shifts each time, is equal to one. There is no padding in convolutional layers. The 2-D convolutional kernel has an equal size along both directions. To ensure the applicability of the convolutional kernel, the input should also be in a square shape. Thus, we added 4 more leads derived from three limb leads (LL for left leg, RA for right arm, LA for left arm): LL-RA-LA; LA-RA-LL; RA-LA-LL; (LL+RA+LA)/3. The last one corresponds to the Wilson central terminal. Along the time dimension, we down-sampled the time courses of QRS (or first half of QRS) to 16 time points before adding noise in simulation. Therefore, each input set of ECGs is a 16 x16 square matrix. This size results in the fast response of both CNNs.

In order to localize the origins of PVCs, we utilized the classification information from two types of CNN: Segment CNN and Epi-Endo CNN. The study diagram of this section is shown in Fig. 14.

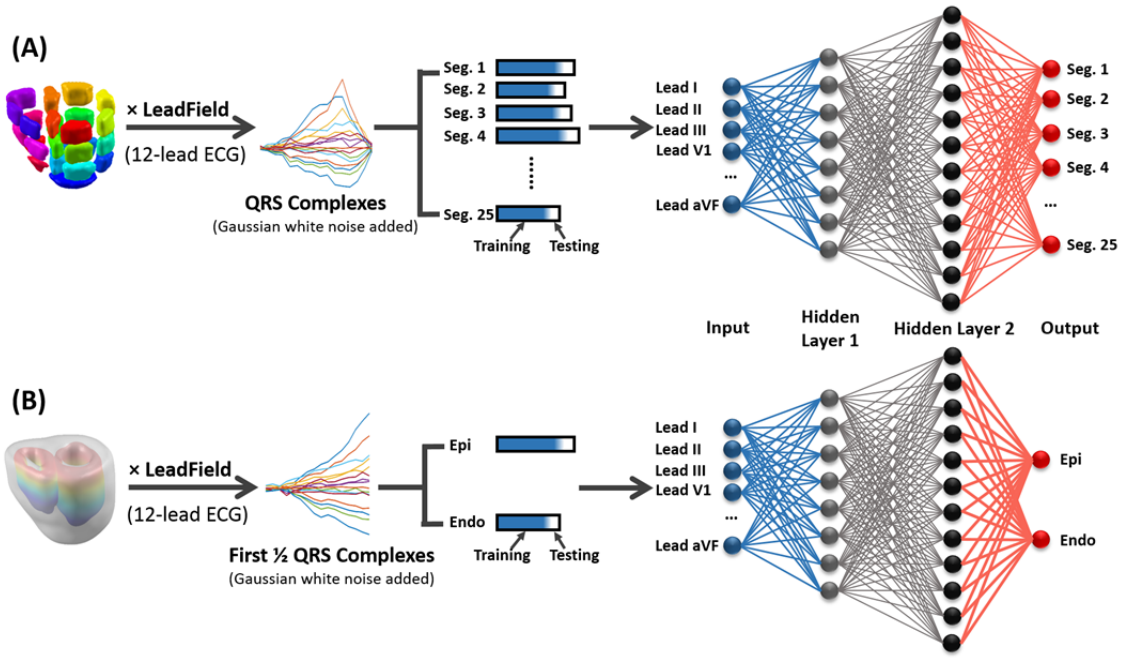

Figure 14 Study diagram of training and testing of convolutional neural network. (A) Segment CNN. All cardiac dipoles are multiplied by the leadfield of 12-lead ECG to get the time courses of electric potentials. Then different levels of Gaussian white noise were added to the potentials. 90% of the QRS complexes (Blue in the bar) from 12-lead ECG were selected as the input to Segment CNN for training procedure. The other 10% (White in the bar) were used for testing. The output of Segment CNN is a probability distribution among 25 segments, the segment with the maximum probability is considered as the output segment. (B) Epi-Endo CNN. Cardiac dipoles located at epicardium and endocardium were selected and multiplied by the leadfield of 12-lead ECG. Different levels of Gaussian white noise were added and the first half of QRS complexes served as the input for Epi-Endo CNN. 90% of the data were for training and the other 10% were for testing. The output is a probability distribution between two output neurons, either neuron 1 (Epi) or neuron 2 (Endo) would have a larger probability.

Segment CNN: The cardiac dipole components resulted from pacing were multiplied by the lead field matrix to generate body surface electrical potentials. Thus, we would have 3,887 sets of 12-lead ECGs corresponding to pacing at 3,887 locations in the ventricular model. QRS complexes were extracted from each lead. A certain level of Gaussian white noise (20 dB, 10 dB or 5 dB) was added to all the leads 10 times to generate noise contaminated 12-lead QRS complexes. Adding a certain level of noise 10 times is for increasing the robustness of Segment CNN to this level of noise since we would have

ample training samples representing different noise variations. In total, our data pool had 38,870 sets of noise-contaminated 12-lead QRS complexes. 10% of the whole data was used for testing, which means 3,887 sets were the testing data. In order to test the CNN without segment bias, within each segment, 155 ($\approx$ 3,887/25) sets of 12-lead QRS complexes were randomly selected each time for testing. The remaining 90% data were used for training procedure. The Segment CNN consisted of 6 layers: Input layer (A set of 12-lead QRS complexes), Hidden layer 1 (convolutional layer with a kernel size of 5), Pooling layer 1 (sampling scale of 1), Hidden layer 2 (convolutional layer with a kernel size of 3), Pooling layer 2 (sampling scale of 2), and Output layer (25 neurons for 25 segments). The batch size was 23, alpha was 1 and the number of epochs was 10. After a ten-fold cross-validation, the accuracy and precision rate of each segment of Segment CNN were calculated.

Epi-Endo CNN: Similar to Segment CNN, 1,709 dipole sources located on epicardium and endocardium were identified and were used to generate single-site pacing 12-lead ECGs. QRS complexes were extracted and the first half of 12-lead QRS complexes was used. Gaussian white noise of a specific SNR was added 10 times. Thus for Epi-Endo CNN, we had 17,090 sets of first half of QRS complexes from 12 leads. 10% of this data was used for testing, which means 855 ($\approx$1,709/2) sets were randomly selected from each category. The remaining 90% data were used for training. The Epi-Endo CNN consisted of 6 layers: Input layer (first half of QRS complexes from 12-lead ECGs), Hidden layer 1 (convolutional layer with a kernel size of 5), Pooling layer 1 (sampling scale of 2), Hidden layer 2 (convolutional layer with a kernel size of 3), Pooling layer 2 (sampling scale of 2), and Output layer (2 neurons corresponding to epicardium and enodcardium). Parameters were set as following: batch size = 25, alpha = 3 and number of epochs = 10. After a ten-fold cross-validation, the accuracy and precision rate of Epi or Endo were calculated.

5.2.4 Localization of Origins of Premature Ventricular Contraction

After training procedures, we tested the localization performance of these two CNNs by feeding a new set of data, which included 12-lead ECGs with a certain SNR resulting from pacing at all possible dipole locations. For each set of 12-lead ECGs, Segment CNN would assign a probability to each segment and Epi-Endo CNN would tell

how possible it was from epicardium or endocardium. Based on these two probability distributions, the estimation of source location was calculated as following:

$$S = \sum_{i=1}^{N} P_i \times (\sum_{j=1}^{2} P_j \times CoG_{ij}) \qquad (5.1)$$

In Eq. (5.1), S is the source location, and P_i is the normalized probability of i^{th} segment and its adjacent segments, the output of Segment CNN. N is the number of adjacent segments each segment has based on the ventricle segmentation in Fig. 13. P_j is the probability of Epi or Endo, the output of Epi-Endo CNN. And j is 1 for Epi; 2 for Endo. CoG_{ij} is the center of gravity of Epi or Endo dipole sources in i^{th} segment.

The segment with the maximum probability from Segment CNN was considered as the output segment. Its adjacent segments (sharing boundaries with the output segment) were determined based on the ventricle segmentation in Fig. 13. The endocardial center of gravity and epicardial center of gravity in each segment were calculated. By multiplying spatial locations of epicardial and endocardial centers of gravity with the probabilities of epicardium and endocardium from Epi-Endo CNN, we obtained epi-endo-informed centers of gravity of the output segment and its adjacent segments. This process corresponds to the multiplication inside the parentheses in Eq. (5.1). Since some dipole sources locate near the boundary of two segments, it was probable that Segment CNN would assign it to its neighboring segment. This is why we took the adjacent segments of an output segment into consideration to decrease the localization error (LE). It was done by first normalizing the output probabilities of Segment CNN only among the output segment and its adjacent segments, and then multiplying the normalized probability with each epi-endo-informed center of gravity. Adding all up, we estimated the source location.

5.2.5 Application to PVC Patients

We collected data from 9 PVC patients (Male = 3, Female = 6, average age = 48.3 ± 12.3 years old). The patient statistics were summarized in Table 1. None of them has undergone ablation procedure before and none of them has structural heart disease. Study protocols were approved by the Institutional Review Board of University of Minnesota and

Shanghai Ruijin Hospital (affiliated with Shanghai Jiao Tong University School of Medicine, Shanghai, China). Written consent forms were obtained from all patients.

Table 6 Patient Statistics of CNN Study

Patient	Age	Gender	Diagnosis	Heart Rate (bpm)	Blood Pressure (mmHg)	Antiarrhythmic Medication	Medical History	PVCs/24 h	Ablation Outcome
1	41	F	PVC	74	116/77	None	Diabetes	15160	RVOT free wall
2	53	M	PVC, RBBB	70	105/63	Bisoprolol	Allergic to penicillin	25630	Left Anterior Fascicle
3	71	F	PVC, Nonsustained AT	70	117/61	Aspirin, Lipitor	Atherosclerosis of coronary artery and carotid artery, cervical disc herniation	21100	RVOT free wall
4	54	F	PVC	80	118/67	Moracizine	Allergic to cephalosporin	13441	RVOT free wall
5	37	M	PVC, Nonsustained VT	95	137/86	None	Sublingual gland excision	27161/23 h	RVOT free wall
6	42	F	PVC	78	115/75	None	None	26337	RVOT free wall
7	43	M	PVC	82	150/80	None	None	39476	RVOT septum
8	33	F	PVC	84	100/55	None	Cardiac arrhythmias, asthma	51226	RVOT free wall
9	61	F	PVC	82	129/79	Amiodarone, Moracizine, metoprolol	Paroxysmal palpitation	8470	RVOT septum

AT = atrial tachycardia, F = female, M = male, PVC = premature ventricular contraction, RBBB = right bundle branch block, RVOT = right ventricular outflow tract, VT = ventricular tachycardia.

For each patient, we had CT images of heart, lungs and torso. Then a boundary element model was built including lungs and torso by using a commercial software (Curry 6.0, Neuroscan, North Carolina, USA). After the segmentation of patient's heart, we registered our ventricular model with it. Prior to the EP study, 208 Ag-AgCl carbon electrodes were placed on the front and back of body surface to record body surface electrical potentials with 2kHz sampling rate for about 10-30 minutes and positions of electrodes were digitized (Fastrak, Polhemus Inc., Colchester, VT, USA). During the recording, all of the patients have spontaneous PVCs recorded and 2 of them also have non-sustained VT detected. Nine electrodes were selected to form 12-lead ECGs later based on their anatomical positions. We registered the generic model with the patient's heart based on the least sum of distances between the two. By using Curry 6.0, the leadfield between these nine electrodes and our generic ventricular model was generated. After the EP study, we also collected CARTO files, which contained spatial locations of successful

ablation sites. CARTO data were registered with the patient's heart based on the landmarks of the geometry of ventricles recorded by the CARTO system. The successful ablation sites are considered as the origins of PVCs in this study.

5.2.6 Statistical Analysis

The accuracy of Segment CNN and Epi-Endo CNN were presented as mean ± SD. The localization error was defined as the spatial distance between the estimated source location and the location of the dipole source in the generic ventricular model that generates the 12-lead ECGs by pacing in simulation, and was defined as the spatial distance between the estimated source location and successful ablation sites in patients' CARTO data.

5.3 Results

Table 7 shows the accuracy and precision of individual segment when Segment CNN was trained and tested on three different Gaussian white noise levels. Accuracy is defined as the percentage of dipole sources being correctly classified within each segment. Precision is defined as when Segment CNN predicts it is in one segment, how often it is correct. Figure 15 shows the precision matrices of Segment CNN. Each column is the precision vector for this segment. When the probability of Segment CNN assigning this segment to other segments is higher than 5%, it is labeled in black in the figure. For example, when trained and tested on 20 dB, for segment 4, Segment CNN would have a relative higher probability of assigning segment 19 and segment 10 to segment 4 even though the precision for segment 4 is 74.1% from Table 7. Table 8 are the precision matrices of Epi-Endo CNN trained and tested under different noise levels.

Table 7 Accuracy and Precision Rates of Segment CNN

	SNR=20 dB		SNR=10 dB		SNR=5 dB	
Unit (%)	Accuracy	Precision	Accuracy	Precision	Accuracy	Precision
1	75.6	72.7	77.0	65.1	63.6	53.9
2	80.5	85.2	61.9	78.4	54.5	70.7
3	78.4	73.9	72.0	61.1	65.7	48.2
4	79.6	74.1	71.6	64.0	56.3	51.2
5	85.7	62.3	80.0	61.6	60.3	46.8
6	83.7	72.4	80.6	68.8	69.0	52.3
7	84.4	79.6	77.4	74.4	59.0	58.3
8	81.5	85.5	71.2	82.3	60.7	74.0
9	89.0	74.6	83.2	66.5	71.2	49.3
10	82.5	73.5	68.4	63.1	46.8	56.7
11	72.5	79.7	67.3	75.3	49.9	63.1
12	62.5	77.5	52.0	73.9	41.7	62.6
13	81.6	75.4	77.4	71.6	58.6	69.8
14	66.5	86.1	65.8	75.5	53.3	61.8
15	79.6	72.7	75.9	70.2	60.5	60.3
16	77.5	83.2	83.5	66.6	77.3	60.8
17	92.6	78.3	80.4	83.7	80.2	54.2
18	58.4	84.0	52.5	75.7	40.4	62.5
19	54.8	91.0	48.5	85.7	25.5	71.4
20	87.1	70.8	84.4	61.7	81.7	52.3
21	81.7	70.4	74.8	62.6	71.6	47.1
22	79.5	75.1	72.7	69.2	63.0	58.8
23	75.4	93.8	62.6	80.9	42.8	77.3
24	62.6	91.1	56.6	88.7	42.9	82.5
25	89.3	89.3	80.2	89.7	57.7	79.0

Table 8 Precision Matrices of Epi-Endo CNN

	SNR=20 dB		SNR=10 dB		SNR=5 dB	
Unit (%)	Epi	Endo	Epi	Endo	Epi	Endo
Epi	85.56	9.94	72.79	18.64	61.36	21.79
Endo	14.44	90.06	27.21	81.36	38.64	78.21

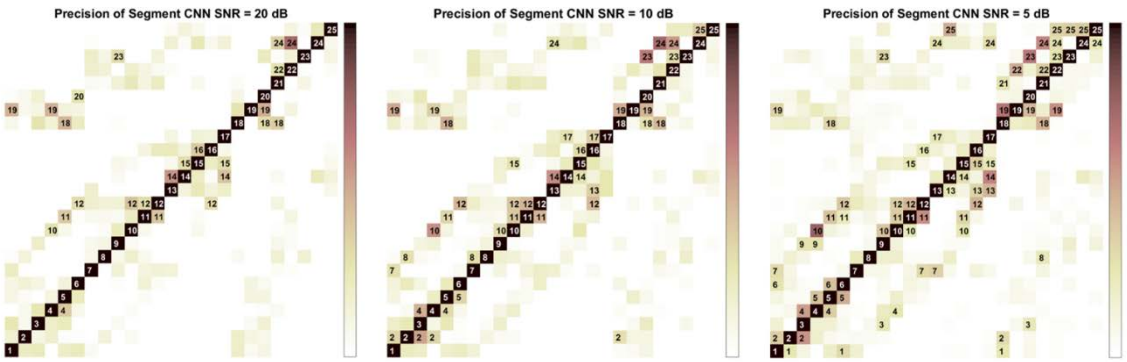

Figure 15 Precision matrix of Segment CNN. Each column represents the precision of this segment over all the other segments. All the blocks with precision higher than 5% are labeled.

When we tested the localization performance of two CNNs, we tested them by feeding them 3,887 new sets of 12-lead ECGs by pacing at a single site with a variety of noise levels (25 dB, 20 dB, 10 dB, 5 dB, 0 dB, -5 dB and -10 dB). Figure 16 presents the LEs along with average accuracies of Segment CNN and Epi-Endo CNN. The left part of the figure is the average LE when Segment CNN and Epi-Endo CNN were tested on 12-lead ECGs from all possible pacing sites in the ventricular model with different noise levels. For example, during the ten-fold cross validation, namely trained and tested on 20 dB 12-lead ECGs, the average accuracy of Epi-Endo CNN was 87.68 % and the average accuracy of Segment CNN was 77.71 %. The middle part and the right part are presented in a similar way as the left part. The exact numbers displayed in Fig. 16 are also in Table 9.

Table 9 Accuracies and Localization Errors of CNNs under Computer Simulation

CNN SNR		**20 dB**	**10 dB**	**5 dB**
Segment Accuracy (%)		77.71±0.01	71.11±0.53	58.18±0.27
EpiEndo Accuracy (%)		87.68±0.61	76.40±0.07	66.20±0.01
Average LE(mm) of Different Data SNR	25 dB	10.37±9.74	10.56±9.73	11.55±9.74
	20 dB	10.43±9.77	10.58±9.74	11.55±9.75
	10 dB	10.76±9.65	10.61±9.64	11.56±9.82
	5 dB	11.38±9.51	10.94±9.68	11.73±9.80
	0 dB	13.09±9.97	11.73±9.65	12.54±9.80
	-5 dB	16.63±11.52	14.32±10.57	14.66±10.36
	-10 dB	22.47±13.28	19.36±11.94	19.96±11.85

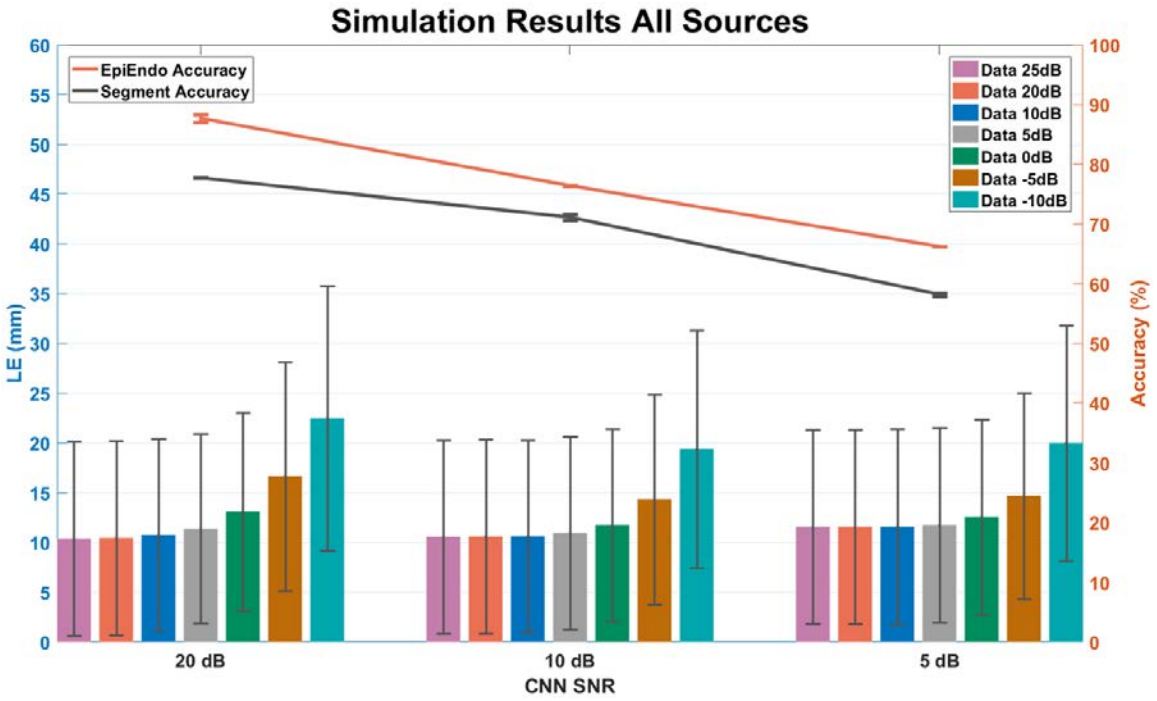

Figure 16 Simulation Results of CNN. The top two lines are the average accuracy of Segment CNN and Epi-Endo CNN trained and tested on 3 different SNR signals. The bottom bars are the average localization errors when applying Segment CNN and Epi-Endo CNN together to data with different SNRs.

5.4 Discussion

This study shows the feasibility of utilizing convolutional neural network to localize origins of PVCs from 12-lead ECGs. We tested the method in both simulation data and clinical patients' data, and obtained good localization errors in both situations.

5.4.1 Properties of Segment CNN and Epi-Endo CNN

The information in Fig. 15, Table 7 and Table 8 could be obtained when we train and test two CNNs on any patient-specific leadfield and under any noise level. It will guide us and give us a prior knowledge of how good two CNNs perform before we feed testing (or clinical) data to calculate the source location. From Fig. 15, we could see as SNR decreases, it is more likely for Segment CNN to assign dipole sources from other segments to one segment, which means the precision rates have dropped. The number of blocks labeled in the precision matrix increases as SNR decreases. Table 8 is the precision matrices of Epi-Endo CNN under different noise level. The common feature of these three

precision matrices is that it is more likely for Epi-Endo CNN to assign sources on endocardial surfaces as epicardial sources. From Table 7, we could know the percentage of dipole sources in each segment that are correctly detected, namely the accuracy of each segment, and also how confident we are in the detection results if one dipole source is predicted to be from some segment.

5.4.2 Localization Errors of CNN

From Fig. 16 and Table 9, we could summarize the following trends of the performance of two CNNs: (1) as SNR drops, the accuracies of both CNNs decrease; (2) as SNR of input data drops, the average LE increases; (3) the average LE is the result of two factors, one is the SNR that two CNNs are trained and tested, the other is the similarity between input data and tested data. The accuracy of Segment CNN of 10 dB is only 6 % less than that of 20 dB. So when the SNR of input data is 10 dB and less than 10 dB, the average LEs of CNNs trained with 10 dB are all smaller than those of CNNs trained with 20 dB. This is when the similarity factor plays a dominant role. However, when the accuracy of Segment CNN drops to 58 %, which is 13 % less than that of 10 dB, the accuracy plays an important role in determining source locations. Because even though input data of 5 dB is more similar to CNNs trained with 5 dB, the average LE is larger than that of CNNs trained with 10 dB and input data of 5 dB. Actually, the average LEs of CNNs trained with 5 dB are all larger than those of CNNs trained with 10 dB. Finally, when we compare the performance between CNNs trained with 20 dB and trained with 5 dB, the average LEs of input data with 0 dB and less of CNNs trained with 5 dB are smaller than those of CNNs trained with 20 dB. This is because even with a much higher training accuracy, CNNs trained with 20 dB fail to classify 12-lead ECGs that are too unlike the training data.

A conclusion from the above simulation results is when the SNR of input data is very low, it is best to train and test CNNs with around 10 dB to minimize LEs; when the SNR of input data is good, it is best to train and test CNNs with a noise level that is the same as the SNR of input data.

5.4.3 Localization Errors of CNN with Heart Registration Errors

Since we register our ventricle current-dipole model with patient's heart, train and test CNNs using this model and finally use CNNs to localize origins of PVCs, it is necessary to investigate the influences of heart registration errors on the localization performance of CNNs. So Fig. 17 shows the average LE when we trained and tested CNNs with correct registration, and applied to localization when the input 12-lead ECGs were generated by the leadfield with heart registration errors. The SNR of training and testing data is the same as the SNR of input data for testing localization performance.

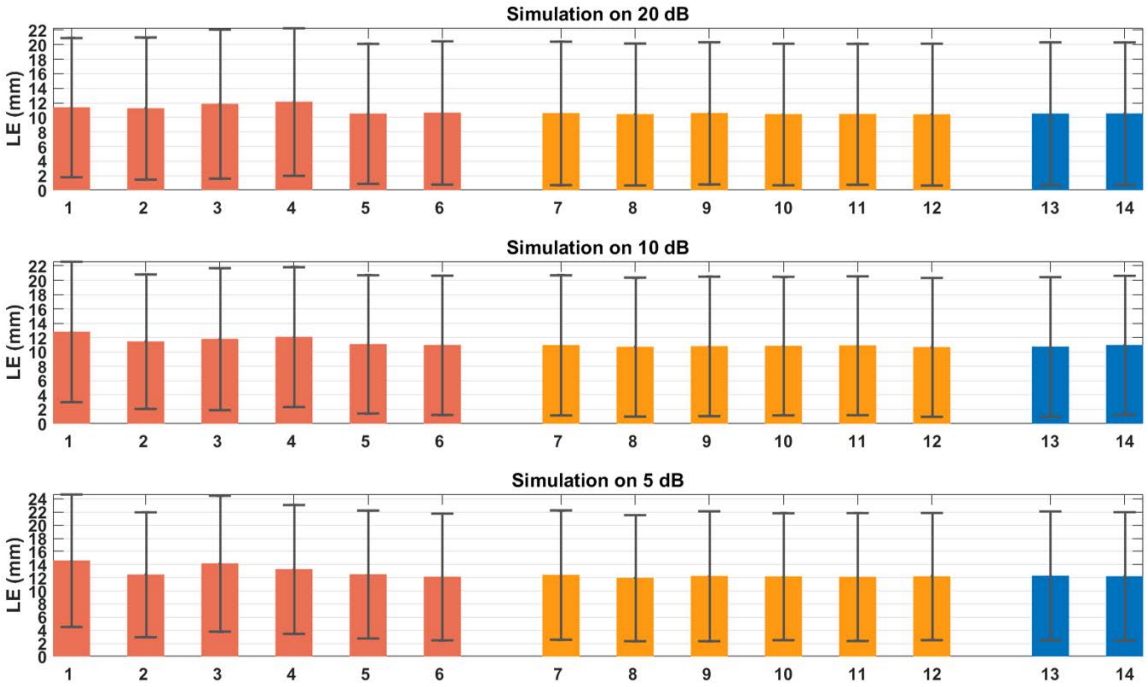

Figure 17 Average localization errors of heart registration errors. 1=Heart move to the right 10 mm; 2=Heart move to the left 10 mm; 3=Heart move up 10 mm; 4=Heart move down 10 mm; 5=Heart move to the anterior 5 mm; 6=Heart move to the posterior 5 mm; 7=Heart rotate right 10°; 8=Heart rotate left 10°; 9=Heart rotate upwards 10°; 10=Heart rotate downwards 10°; 11=Heart rotate clockwise 10°; 12=Heart rotate counterclockwise 10°; 13= Heart inflated 10 mm; 14=Heart deflated 10 mm.

Three categories of heart registration errors were investigated: shift, rotation and scaling. Overall, all the average LEs are larger than those of correct registration. Within shift group, because heart is already very close to the front body surface, so we could only move heart forward by 5 mm. For comparison purpose, we also moved heart backwards by

5 mm. Heart moving to the right always generated a larger LE than moving to the left. Within rotation group, heart rotating to the right always generated a larger LE than rotating to the left. Within scaling group, there is no obvious trend. Among all the registration errors, we found that shift group gave higher LEs than the other two groups on average.

Based on the above analysis of the registration error results, we should pay attention when we need to shift the ventricular model for the registration with patient's heart. And CNNs are generally robust to a variety of heart registration errors if we compare these LEs with those that are from correct registrations: 10.43 ± 9.77 mm (20 dB), 10.61 ± 9.64 mm (10 dB) and 11.73 ± 9.80 mm (5 dB). Generally, the above heart registration errors would increase average LE by 1 to 2 mm.

5.4.4 Application to PVC Patients

From the last column in Table 6, which is the ablation record from CARTO files, the origins of PVC lied in different regions in the ventricles, 1 patient had PVC originated from the left anterior fascicle, 6 patients were ablated at free-wall side of right ventricular outflow tract, and PVCs in the left 2 patients were detected in the septal side of right ventricular outflow tract. On average, the localization error of 9 patients is 10.9 ± 5.5 mm, which is good and reasonable considering the source location was estimated solely from 12-lead ECGs. The average median registration error is 2.4 ± 0.2 mm. Registration error is one factor that contributes to the final localization error. Patients' results were summarized in Fig. 18. The present results demonstrated the feasibility of employing a generic anisotropic ventricle current-dipole model to mimic cardiac activities in a patient without structural heart disease. Generally, the more similar a patient's heart is with the ventricular model, the more accurate the predictions will be. And this also shows the capability of our method to estimate origins of PVCs from different areas.

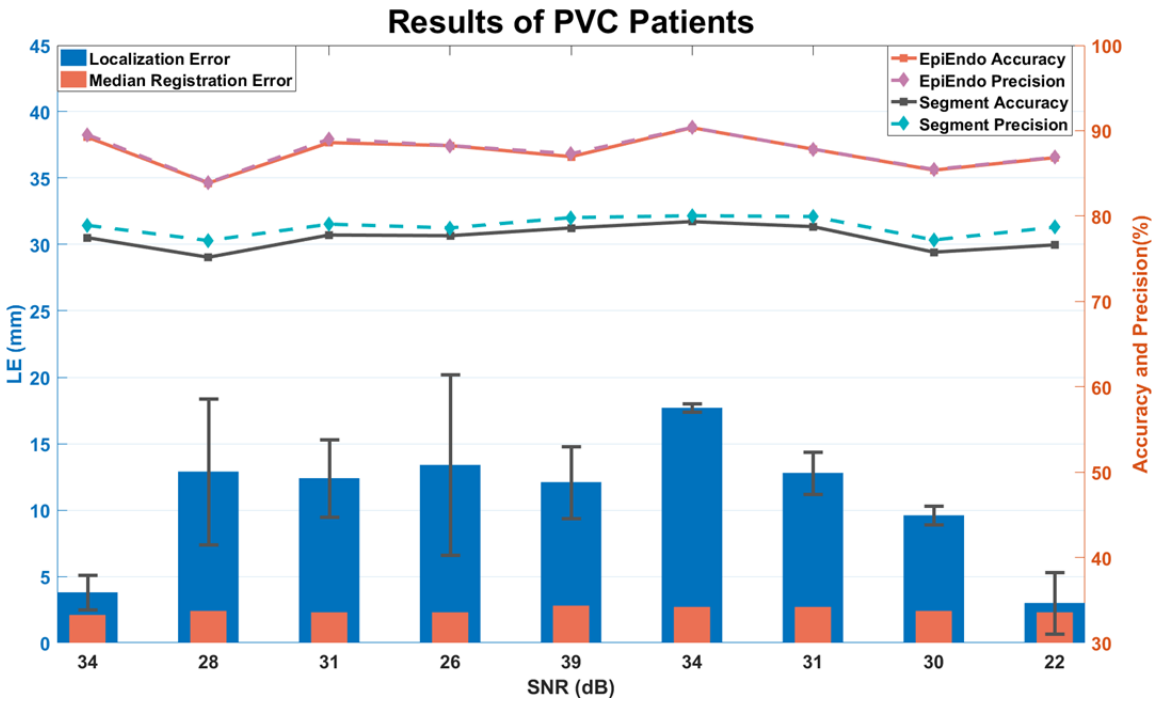

Figure 18 Results of PVC patients. The right y axis represents the accuracy and average precision rate of the trained Segment CNN and Epi-Endo CNN. And the left y axis shows the average localization error of 10 PVCs from each of 9 patients (blue bars). The orange bars represent the median registration error between the general model and patient's heart geometry. On the bottom, x axis is the noise level estimated from 12-lead ECGs and is also the noise level we trained and tested the CNNs by adding Gaussian white noise.

5.4.5 Merits and Limitations

Merits: This method can be applied to the localization of PVC and focal ventricular tachycardia (VT) since the training data is generated from single-site pacing. It is a stable method in the sense of two-fold: once CNNs are trained on a patient, they are applicable to all the other PVCs and focal VTs from the same patient; structures and parameters of both CNNs all remain the same across different subjects and noise levels. It is a robust method because average LEs under different noise levels and heart registration errors fluctuate in a range of 1 to 2 mm. Since a generic ventricle current-dipole model is used, this method does not require high-resolution contrast cardiac CT images. Anatomical CT images show the shape and orientation of ventricles are good enough for the registration purpose. Thus, we reduce patients' burden by avoiding injecting contrast into the body. Training and testing of CNNs could be done off-line prior to the EP study and it generally takes about

20 minutes. The total analysis time including building the boundary element model, registration of the ventricular model, calculating the leadfield between electrodes and ventricular model, and training and testing CNNs would not be longer than 2 hours in a 64-bit operating system with 3.40 GHz Intel i7 processor. Once CNNs have been trained, it would take 0.2 s to calculate the source location given QRS complexes from 12-lead ECGs. Other than the previous methods that require calculating statistical features from 12-lead ECGs, some expertise of recognizing patterns from 12-lead ECGs, and are usually limited in the types of ventricular arrhythmias, the method we present here is easy to implement, relieves the burden on electrophysiology specialists, and finally helps guide ablation procedure by providing potential source locations throughout the ventricles.

Limitations: Because it is a single-site pacing ventricle current-dipole model, this method is not applicable to multisite excitation activities and reentry VT. The sources of localization errors mainly come from two places: one is the registration between the ventricular model and patient's heart, the other is the registration of 12-lead electrodes. While the latter can be reduced by digitizing more anatomical landmarks to help in the registration of electrodes, the former is somehow unavoidable because we use a generic ventricular model. In the future, we could employ a personalized cardiac electrophysiology model as have been used in cardiac electrical imaging studies [140] to overcome the first source of localization errors.

Chapter 6

Conclusions and Future Work

6.1 Conclusions

In chapter 3, we have proposed a novel imaging method (SSF) that reconstructs activation sequences in focal and reentrant VTs by formulating and solving the inverse problem in the frequency domain. We have evaluated the performance of SSF through focal VT simulation under a variety of noise levels and SSF achieved better results than WMN on average. We have applied SSF to reentrant VTs in a late myocardial infarction swine model, and successfully depicted the reentrant circuits in four reentrant VTs. The localization of the conduction block and central pathways was supported by previous works. Noninvasively detecting the central pathway and the exit site of a reentry circuit would save the patient from undergoing prolonged procedure and result in a smaller yet accurate ablation region.

In chapter 4, we have extended the application of 3DCEI by developing 3D ARI imaging to image the repolarization process in the heart. Our results are promising suggesting the possibility of using ARI imaging to localize origins of PVCs in PVC patients with normal structure. The good correlation and relative low localization errors as compared with last ablation sites suggest that ARI imaging could be an alternative of evaluating global dispersion of ventricular repolarization and detecting potential ablation targets in EP studies.

In chapter 5, we have proposed a novel method to localize the site of origin of premature ventricular contractions from 12-lead ECG using convolutional neural networks and a realistic anisotropic ventricle computer model. We have evaluated our method under various numerical experiments, and achieved a good overall performance. By applying it to real data in a group of nine patients, we have shown the capability of our method to target the potential ablation site in premature ventricular contractions patients. This work suggests a new approach for cardiac source localization of origin of arrhythmias using only the 12-lead ECG by means of CNN.

6.2 Future Work

In the future, we will test SSF thoroughly in more cases that are complicated. We will evaluate the performance of SSF in animal models with other types of myocardial infarction. Regarding the size of the reentry circuit, we have shown that SSF could reconstruct the reentry circuit of a macroreentry. Whether it could detect a microreentry remains unknown. In addition, in some complicated cases, multiple reentry circuits may exist. Whether SSF could image multiple circuits simultaneously needs to be tested in the future. When a microreentry is too small, it appears as a “focal” VT. The simulation study has demonstrated the capability of SSF in reconstructing activation sequences of focal VTs under different noise levels. In summary, we see SSF as a promising tool of reconstructing 3D activation sequences of ventricular arrhythmias. Further investigation in animal models or in patients will prove its strength or limitations in application.

3D ARI imaging can be potentially applied to any condition that involves repolarization abnormalities in the ventricles. This may include but not limited to: bundle branch block, early repolarization, cardiac memory, Wolff-Parkinson-White syndrome and ischemia. In addition, to reflect the dynamic changes of repolarization and to validate 3D ARI imaging, a simultaneous recording of BSPM and clinical recordings (contact or noncontact unipolar electrograms) will be preferred. Further investigation is necessary to test the applicability and performance of 3D ARI imaging under these situations.

Using CNN and a generic ventricle computer model to localize origins of premature ventricular contractions has the advantage of saving analysis time and being fast in response. Thus, applications for real-time monitoring and guiding ablation procedure in the future would be a reasonable step towards the commercialization of this method.

References

[1] E. P. Widmaier, H. Raff, and K. T. Strang, "Vander's human physiology," *Mech. Body Funct.*, 2011.

[2] J. L. Hudson and T. T. Tsotsis, "Electrochemical reaction dynamics: a review," *Chem. Eng. Sci.*, vol. 49, no. 10, pp. 1493–1572, 1994.

[3] E. M. Aliot *et al.*, "EHRA/HRS Expert Consensus on Catheter Ablation of Ventricular ArrhythmiasDeveloped in a partnership with the European Heart Rhythm Association (EHRA), a Registered Branch of the European Society of Cardiology (ESC), and the Heart Rhythm Society (HRS); in collaboration with the American College of Cardiology (ACC) and the American Heart Association (AHA)," *EP Eur.*, vol. 11, no. 6, pp. 771–817, Jun. 2009.

[4] K. P. Letsas *et al.*, "Methods and indications for ablation of ventricular tachycardia," *Hell. J Cardiol*, vol. 52, pp. 427–436, 2011.

[5] A. Arya, C. Piorkowski, P. Sommer, J.-H. Gerds-Li, H. Kottkamp, and G. Hindricks, "Idiopathic outflow tract tachycardias," *Herz*, vol. 32, no. 3, pp. 218–225, 2007.

[6] W. G. Stevenson and K. Soejima, "Catheter ablation for ventricular tachycardia," *Circulation*, vol. 115, no. 21, pp. 2750–2760, 2007.

[7] R. J. Simpson, W. E. Cascio, P. J. Schreiner, R. S. Crow, P. M. Rautaharju, and G. Heiss, "Prevalence of premature ventricular contractions in a population of African American and white men and women: the Atherosclerosis Risk in Communities (ARIC) study," *Am. Heart J.*, vol. 143, no. 3, pp. 535–540, 2002.

[8] B. Taccardi, "Distribution of heart potentials on the thoracic surface of normal human subjects," *Circ. Res.*, vol. 12, no. 4, pp. 341–352, 1963.

[9] J. A. Abildskov, M. J. Burgess, R. L. Lux, and R. F. Wyatt, "Experimental evidence for regional cardiac influence in body surface isopotential maps of dogs.," *Circ. Res.*, vol. 38, no. 5, pp. 386–391, 1976.

[10] D. M. Mirvis, *Body surface electrocardiographic mapping*, vol. 82. Springer Science & Business Media, 2012.

[11] M. Akahoshi *et al.*, "Body-surface distribution of changes in activation-recovery intervals before and after catheter ablation in patients with Wolff-Parkinson-White syndrome," *Circulation*, vol. 96, no. 5, pp. 1566–1574, 1997.

[12] Y. Okamoto, Y. Teramachi, and T. Musha, "Limitation of the inverse problem in body surface potential mapping," *IEEE Trans. Biomed. Eng.*, no. 11, pp. 749–754, 1983.

[13] L. S. Klein, H. T. Shih, F. K. Hackett, D. P. Zipes, and W. M. Miles, "Radiofrequency catheter ablation of ventricular tachycardia in patients without structural heart disease.," *Circulation*, vol. 85, no. 5, pp. 1666–1674, May 1992.

[14] F. E. Marchlinski, D. J. Callans, C. D. Gottlieb, and E. Zado, "Linear ablation lesions for control of unmappable ventricular tachycardia in patients with ischemic and nonischemic cardiomyopathy," *Circulation*, vol. 101, no. 11, pp. 1288–1296, 2000.

[15] A. Arenal *et al.*, "Tachycardia-related channel in the scar tissue in patients with sustained monomorphic ventricular tachycardias," *Circulation*, vol. 110, no. 17, pp. 2568–2574, 2004.

[16] R. C. Barr and M. S. Spach, "Inverse calculation of QRS-T epicardial potentials from body surface potential distributions for normal and ectopic beats in the intact dog.," *Circ. Res.*, vol. 42, no. 5, pp. 661–675, 1978.

[17] R. M. Gulrajani, F. A. Roberge, and P. Savard, "Moving dipole inverse ECG and EEG solutions," *IEEE Trans. Biomed. Eng.*, no. 12, pp. 903–910, 1984.

[18] H. S. Oster, B. Taccardi, R. L. Lux, P. R. Ershler, and Y. Rudy, "Noninvasive Electrocardiographic Imaging," *Circulation*, vol. 96, no. 3, pp. 1012–1024, Aug. 1997.

[19] G. Li and B. He, “Localization of the site of origin of cardiac activation by means of a heart-model-based electrocardiographic imaging approach,” *IEEE Trans. Biomed. Eng.*, vol. 48, no. 6, pp. 660–669, 2001.
[20] B. He, G. Li, and X. Zhang, “Noninvasive three-dimensional activation time imaging of ventricular excitation by means of a heart-excitation model,” *Phys. Med. Biol.*, vol. 47, no. 22, p. 4063, 2002.
[21] B. Tilg *et al.*, “Model-based imaging of cardiac electrical excitation in humans,” *IEEE Trans. Med. Imaging*, vol. 21, no. 9, pp. 1031–1039, 2002.
[22] B. He, G. Li, and X. Zhang, “Noninvasive imaging of cardiac transmembrane potentials within three-dimensional myocardium by means of a realistic geometry anisotropic heart model,” *IEEE Trans. Biomed. Eng.*, vol. 50, no. 10, pp. 1190–1202, 2003.
[23] A. A. Armoundas, A. B. Feldman, R. Mukkamala, and R. J. Cohen, “A single equivalent moving dipole model: an efficient approach for localizing sites of origin of ventricular electrical activation,” *Ann. Biomed. Eng.*, vol. 31, no. 5, pp. 564–576, 2003.
[24] F. Greensite, “Heart surface electrocardiographic inverse solutions,” *Model. Imaging Bioelectrical Act. Princ. Appl. N. Y. Kluwer Acad. Publ.*, pp. 119–160, 2004.
[25] D. Farina, Y. Jiang, O. Skipa, O. Dossel, C. Kaltwasser, and W. R. Bauer, “The use of the simulation results as a priori information to solve the inverse problem of electrocardiography for a patient,” in *Computers in Cardiology, 2005*, 2005, pp. 571–574.
[26] Z. Liu, C. Liu, and B. He, “Noninvasive reconstruction of three-dimensional ventricular activation sequence from the inverse solution of distributed equivalent current density,” *IEEE Trans. Med. Imaging*, vol. 25, no. 10, pp. 1307–1318, Oct. 2006.
[27] T. Berger *et al.*, “Single-Beat Noninvasive Imaging of Cardiac Electrophysiology of Ventricular Pre-Excitation,” *J. Am. Coll. Cardiol.*, vol. 48, no. 10, pp. 2045–2052, Nov. 2006.
[28] O. Dossel, W. R. Bauer, D. Farina, C. Kaltwasser, and O. Skipa, “Imaging of bioelectric sources in the heart using a cellular automaton model,” in *Engineering in Medicine and Biology Society, 2005. IEEE-EMBS 2005. 27th Annual International Conference of the*, 2006, pp. 1067–1070.
[29] B. F. Nielsen, X. Cai, and M. Lysaker, “On the possibility for computing the transmembrane potential in the heart with a one shot method: An inverse problem,” *Math. Biosci.*, vol. 210, no. 2, pp. 523–553, 2007.
[30] B. F. Nielsen, M. Lysaker, and A. Tveito, “On the use of the resting potential and level set methods for identifying ischemic heart disease: An inverse problem,” *J. Comput. Phys.*, vol. 220, no. 2, pp. 772–790, 2007.
[31] C. Liu, N. D. Skadsberg, S. E. Ahlberg, C. M. Swingen, P. A. Iaizzo, and B. He, “Estimation of Global Ventricular Activation Sequences by Noninvasive Three-Dimensional Electrical Imaging: Validation Studies in a Swine Model During Pacing,” *J. Cardiovasc. Electrophysiol.*, vol. 19, no. 5, pp. 535–540, 2008.
[32] C. Han, Z. Liu, X. Zhang, S. Pogwizd, and B. He, “Noninvasive three-dimensional cardiac activation imaging from body surface potential maps: a computational and experimental study on a rabbit model,” *IEEE Trans. Med. Imaging*, vol. 27, no. 11, pp. 1622–1630, 2008.
[33] D. Lai, C. Liu, M. D. Eggen, P. A. Iaizzo, and B. He, “Equivalent moving dipole localization of cardiac ectopic activity in a swine model during pacing,” *IEEE Trans. Inf. Technol. Biomed.*, vol. 14, no. 6, pp. 1318–1326, 2010.
[34] L. Wang, H. Zhang, K. C. Wong, H. Liu, and P. Shi, “Physiological-model-constrained noninvasive reconstruction of volumetric myocardial transmembrane potentials,” *IEEE Trans. Biomed. Eng.*, vol. 57, no. 2, pp. 296–315, 2010.
[35] L. Wang, K. C. Wong, H. Zhang, H. Liu, and P. Shi, “Noninvasive computational imaging of cardiac electrophysiology for 3-D infarct,” *IEEE Trans. Biomed. Eng.*, vol. 58, no. 4, pp. 1033–1043, 2011.

[36] Y. Wang *et al.*, "Noninvasive electroanatomic mapping of human ventricular arrhythmias with electrocardiographic imaging," *Sci. Transl. Med.*, vol. 3, no. 98, p. 98ra84–98ra84, 2011.
[37] C. Han, S. M. Pogwizd, C. R. Killingsworth, and B. He, "Noninvasive reconstruction of the three-dimensional ventricular activation sequence during pacing and ventricular tachycardia in the canine heart," *Am. J. Physiol.-Heart Circ. Physiol.*, vol. 302, no. 1, pp. H244–H252, 2012.
[38] C. Liu, M. D. Eggen, C. M. Swingen, P. A. Iaizzo, and B. He, "Noninvasive mapping of transmural potentials during activation in swine hearts from body surface electrocardiograms," *IEEE Trans. Med. Imaging*, vol. 31, no. 9, pp. 1777–1785, 2012.
[39] L. Wang *et al.*, "Transmural imaging of ventricular action potentials and post-infarction scars in swine hearts," *IEEE Trans. Med. Imaging*, vol. 32, no. 4, pp. 731–747, 2013.
[40] L. Wang, "Computational reduction for noninvasive transmural electrophysiological imaging," *Comput. Biol. Med.*, vol. 43, no. 3, pp. 184–199, 2013.
[41] A. Rahimi, J. Xu, and L. Wang, "-Norm Regularization in Volumetric Imaging of Cardiac Current Sources," *Comput. Math. Methods Med.*, vol. 2013, 2013.
[42] B. F. Nielsen, M. Lysaker, and P. Grøttum, "Computing ischemic regions in the heart with the bidomain model—first steps towards validation," *IEEE Trans. Med. Imaging*, vol. 32, no. 6, pp. 1085–1096, 2013.
[43] C. Han, S. M. Pogwizd, C. R. Killingsworth, Z. Zhou, and B. He, "Noninvasive cardiac activation imaging of ventricular arrhythmias during drug-induced QT prolongation in the rabbit heart," *Heart Rhythm*, vol. 10, no. 10, pp. 1509–1515, 2013.
[44] B. Erem, J. Coll-Font, R. M. Orellana, P. St'ovicek, and D. H. Brooks, "Using transmural regularization and dynamic modeling for noninvasive cardiac potential imaging of endocardial pacing with imprecise thoracic geometry," *IEEE Trans. Med. Imaging*, vol. 33, no. 3, pp. 726–738, 2014.
[45] J. Xu, A. R. Dehaghani, F. Gao, and L. Wang, "Noninvasive transmural electrophysiological imaging based on minimization of total-variation functional," *IEEE Trans. Med. Imaging*, vol. 33, no. 9, pp. 1860–1874, 2014.
[46] Z. Zhou, C. Han, T. Yang, and B. He, "Noninvasive Imaging of 3-Dimensional Myocardial Infarction From the Inverse Solution of Equivalent Current Density in Pathological Hearts," *IEEE Trans. Biomed. Eng.*, vol. 62, no. 2, pp. 468–476, Feb. 2015.
[47] C. Han, S. M. Pogwizd, L. Yu, Z. Zhou, C. R. Killingsworth, and B. He, "Imaging cardiac activation sequence during ventricular tachycardia in a canine model of nonischemic heart failure," *Am. J. Physiol.-Heart Circ. Physiol.*, vol. 308, no. 2, pp. H108–H114, 2015.
[48] B. M. Horáček, L. Wang, F. Dawoud, J. Xu, and J. L. Sapp, "Noninvasive electrocardiographic imaging of chronic myocardial infarct scar," *J. Electrocardiol.*, vol. 48, no. 6, pp. 952–958, 2015.
[49] L. Yu, Z. Zhou, and B. He, "Temporal sparse promoting three dimensional imaging of cardiac activation," *IEEE Trans. Med. Imaging*, vol. 34, no. 11, pp. 2309–2319, 2015.
[50] Z. Zhou, Q. Jin, L. Y. Chen, L. Yu, L. Wu, and B. He, "Noninvasive Imaging of High-Frequency Drivers and Reconstruction of Global Dominant Frequency Maps in Patients With Paroxysmal and Persistent Atrial Fibrillation," *IEEE Trans. Biomed. Eng.*, vol. 63, no. 6, pp. 1333–1340, 2016.
[51] B. He, C. Liu, and Y. Zhang, "Three-dimensional cardiac electrical imaging from intracavity recordings," *IEEE Trans. Biomed. Eng.*, vol. 54, no. 8, pp. 1454–1460, 2007.
[52] C. Liu, P. A. Iaizzo, and B. He, "Three-dimensional imaging of ventricular activation and electrograms from intracavitary recordings," *IEEE Trans. Biomed. Eng.*, vol. 58, no. 4, pp. 868–875, 2011.
[53] W. T. Miller and D. B. Geselowitz, "Simulation studies of the electrocardiogram. I. The normal heart.," *Circ. Res.*, vol. 43, no. 2, pp. 301–315, 1978.

[54] L. Tung, “A bi-domain model for describing ischemic myocardial dc potentials.,” Massachusetts Institute of Technology, 1978.
[55] D. B. Geselowitz and W. T. Miller III, “A bidomain model for anisotropic cardiac muscle,” *Ann. Biomed. Eng.*, vol. 11, no. 3–4, pp. 191–206, 1983.
[56] Y. Yamashita and D. B. Geselowitz, “Source-field relationships for cardiac generators on the heart surface based on their transfer coefficients,” *IEEE Trans. Biomed. Eng.*, no. 11, pp. 964–970, 1985.
[57] A. Natale *et al.*, “Venice Chart International Consensus Document on Ventricular Tachycardia/Ventricular Fibrillation Ablation,” *J. Cardiovasc. Electrophysiol.*, vol. 21, no. 3, pp. 339–379, Mar. 2010.
[58] A. Gramfort, D. Strohmeier, J. Haueisen, M. S. Hämäläinen, and M. Kowalski, “Time-frequency mixed-norm estimates: Sparse M/EEG imaging with non-stationary source activations,” *NeuroImage*, vol. 70, pp. 410–422, 2013.
[59] S. Castaño-Candamil, J. Höhne, J.-D. Martínez-Vargas, X.-W. An, G. Castellanos-Domínguez, and S. Haufe, “Solving the EEG inverse problem based on space–time–frequency structured sparsity constraints,” *NeuroImage*, vol. 118, pp. 598–612, 2015.
[60] O. Jensen and S. Vanni, “A new method to identify multiple sources of oscillatory activity from magnetoencephalographic data,” *Neuroimage*, vol. 15, no. 3, pp. 568–574, 2002.
[61] H. Yuan, A. Doud, A. Gururajan, and B. He, “Cortical imaging of event-related (de) synchronization during online control of brain-computer interface using minimum-norm estimates in frequency domain,” *IEEE Trans. Neural Syst. Rehabil. Eng.*, vol. 16, no. 5, pp. 425–431, 2008.
[62] P. C. Hansen, “Analysis of discrete ill-posed problems by means of the L-curve,” *SIAM Rev.*, vol. 34, no. 4, pp. 561–580, 1992.
[63] P. C. Hansen and D. P. O’Leary, “The use of the L-curve in the regularization of discrete ill-posed problems,” *SIAM J. Sci. Comput.*, vol. 14, no. 6, pp. 1487–1503, 1993.
[64] M. Grant and S. Boyd, “Graph implementations for nonsmooth convex programs,” *Recent Adv. Learn. Control*, pp. 95–110, 2008.
[65] S. M. Pogwizd and P. B. Corr, “Electrophysiologic mechanisms underlying arrhythmias due to reperfusion of ischemic myocardium.,” *Circulation*, vol. 76, no. 2, pp. 404–426, 1987.
[66] S. M. Pogwizd and P. B. Corr, “Reentrant and nonreentrant mechanisms contribute to arrhythmogenesis during early myocardial ischemia: results using three-dimensional mapping.,” *Circ. Res.*, vol. 61, no. 3, pp. 352–371, Sep. 1987.
[67] N. El-Sherif, R. A. Smith, and K. Evans, “Canine ventricular arrhythmias in the late myocardial infarction period. 8. Epicardial mapping of reentrant circuits.,” *Circ. Res.*, vol. 49, no. 1, pp. 255–265, 1981.
[68] R. Mehra, R. H. Zeiler, W. B. Gough, and N. El-Sherif, “Reentrant ventricular arrhythmias in the late myocardial infarction period. 9. Electrophysiologic-anatomic correlation of reentrant circuits.,” *Circulation*, vol. 67, no. 1, pp. 11–24, 1983.
[69] N. El-Sherif, W. B. Gough, R. H. Zeiler, and R. Hariman, “Reentrant ventricular arrhythmias in the late myocardial infarction period. 12. Spontaneous versus induced reentry and intramural versus epicardial circuits,” *J. Am. Coll. Cardiol.*, vol. 6, no. 1, pp. 124–132, 1985.
[70] W. B. Gough, R. Mehra, M. Restivo, R. H. Zeiler, and N. El-Sherif, “Reentrant ventricular arrhythmias in the late myocardial infarction period in the dog. 13. Correlation of activation and refractory maps.,” *Circ. Res.*, vol. 57, no. 3, pp. 432–442, 1985.
[71] N. EL-SHERIF, W. B. GOUGH, and M. RESTIVO, “Reentrant ventricular arrhythmias in the late myocardial infarction period: 14. Mechanisms of resetting, entrainment, acceleration, or termination of reentrant tachycardia by programmed electrical stimulation,” *Pacing Clin. Electrophysiol.*, vol. 10, no. 2, pp. 341–371, 1987.

[72] N. El-Sherif, W. B. Gough, and M. Restivo, “Reentrant ventricular arrhythmias in the late myocardial infarction period: mechanism by which a short-long-short cardiac sequence facilitates the induction of reentry.,” *Circulation*, vol. 83, no. 1, pp. 268–278, 1991.
[73] J. M. De Bakker *et al.*, “Macroreentry in the infarcted human heart: the mechanism of ventricular tachycardias with a ‘focal’ activation pattern,” *J. Am. Coll. Cardiol.*, vol. 18, no. 4, pp. 1005–1014, 1991.
[74] J. J. Fenoglio Jr, T. D. Pham, A. H. Harken, L. N. Horowitz, M. E. Josephson, and A. L. Wit, “Recurrent sustained ventricular tachycardia: structure and ultrastructure of subendocardial regions in which tachycardia originates,” *Josephson Sch. Leg. Important Contrib. Electrophysiol.*, vol. 68, no. 3, p. 187, 2015.
[75] J. M. De Bakker *et al.*, “Reentry as a cause of ventricular tachycardia in patients with chronic ischemic heart disease: electrophysiologic and anatomic correlation.,” *Circulation*, vol. 77, no. 3, pp. 589–606, 1988.
[76] W. G. Stevenson *et al.*, “Exploring postinfarction reentrant ventricular tachycardia with entrainment mapping,” *J. Am. Coll. Cardiol.*, vol. 29, no. 6, pp. 1180–1189, 1997.
[77] J. E. Burnes, B. Taccardi, R. S. MacLeod, and Y. Rudy, “Noninvasive ECG imaging of electrophysiologically abnormal substrates in infarcted hearts,” *Circulation*, vol. 101, no. 5, pp. 533–540, 2000.
[78] J. E. Burnes, B. Taccardi, and Y. Rudy, “A noninvasive imaging modality for cardiac arrhythmias,” *Circulation*, vol. 102, no. 17, pp. 2152–2158, 2000.
[79] J. E. Burnes, B. Taccardi, P. R. Ershler, and Y. Rudy, “Noninvasive electrocardiogram imaging of substrate and intramural ventricular tachycardia in infarcted hearts,” *J. Am. Coll. Cardiol.*, vol. 38, no. 7, pp. 2071–2078, 2001.
[80] K. R. Laurita, S. D. Girouard, F. G. Akar, and D. S. Rosenbaum, “Modulated dispersion explains changes in arrhythmia vulnerability during premature stimulation of the heart,” *Circulation*, vol. 98, no. 24, pp. 2774–2780, 1998.
[81] J. Han, P. G. De Jalon, and G. K. Moe, “Adrenergic effects on ventricular vulnerability,” *Circ. Res.*, vol. 14, no. 6, pp. 516–524, 1964.
[82] J. Han and G. K. Moe, “Nonuniform recovery of excitability in ventricular muscle,” *Circ. Res.*, vol. 14, no. 1, pp. 44–60, 1964.
[83] J. Han, D. Millet, B. Chizzonitti, and G. K. Moe, “Temporal dispersion of recovery of excitability in atrium and ventricle as a function of heart rate,” *Am. Heart J.*, vol. 71, no. 4, pp. 481–487, 1966.
[84] J. Han, G. de Jalon, and G. K. Moe, “Fibrillation threshold of premature ventricular responses,” *Circ. Res.*, vol. 18, no. 1, pp. 18–25, 1966.
[85] J. Han, J. DeTraglia, D. Millet, and G. K. Moe, “Incidence of ectopic beats as a function of basic rate in the ventricle,” *Am. Heart J.*, vol. 72, no. 5, pp. 632–639, 1966.
[86] V. S. Chauhan *et al.*, “Increased ventricular repolarization heterogeneity in patients with ventricular arrhythmia vulnerability and cardiomyopathy: a human in vivo study,” *Am. J. Physiol.-Heart Circ. Physiol.*, vol. 290, no. 1, pp. H79–H86, 2006.
[87] R. F. Wyatt, “COMPARISON OF ESTIMATES OF ACTIVATION AND RECOVERY TIMES FROM BIPOLAR AND UNIPOLAR ELECTROGRAMS TO INVIVO TRANSMEMBRANE ACTION-POTENTIAL DURATIONS,” in *IEEE TRANSACTIONS ON BIOMEDICAL ENGINEERING*, 1980, vol. 27, pp. 528–529.
[88] R. F. Wyatt, M. J. Burgess, A. K. Evans, R. L. Lux, J. A. Abildskov, and T. Tsutsumi, “Estimation of ventricular transmembrane action potential durations and repolarization times from unipolar electrograms,” *Am. J. Cardiol.*, vol. 47, p. 488, 1981.
[89] C. K. Millar, F. A. Kralios, and R. L. Lux, “Correlation between refractory periods and activation-recovery intervals from electrograms: effects of rate and adrenergic interventions.,” *Circulation*, vol. 72, no. 6, pp. 1372–1379, 1985.

[90] C. W. Haws and R. L. Lux, “Correlation between in vivo transmembrane action potential durations and activation-recovery intervals from electrograms. Effects of interventions that alter repolarization time.,” *Circulation*, vol. 81, no. 1, pp. 281–288, 1990.
[91] P.-S. Chen *et al.*, “Epicardial activation and repolarization patterns in patients with right ventricular hypertrophy.,” *Circulation*, vol. 83, no. 1, pp. 104–118, 1991.
[92] L. Gepstein, G. Hayam, and S. A. Ben-Haim, “Activation-repolarization coupling in the normal swine endocardium,” *Circulation*, vol. 96, no. 11, pp. 4036–4043, 1997.
[93] A. M. Yue, J. R. Paisey, S. Robinson, T. R. Betts, P. R. Roberts, and J. M. Morgan, “Determination of human ventricular repolarization by noncontact mapping,” *Circulation*, vol. 110, no. 11, pp. 1343–1350, 2004.
[94] R. Coronel *et al.*, “Monophasic action potentials and activation recovery intervals as measures of ventricular action potential duration: experimental evidence to resolve some controversies,” *Heart Rhythm*, vol. 3, no. 9, pp. 1043–1050, 2006.
[95] M. Potse, A. Vinet, T. Opthof, and R. Coronel, “Validation of a simple model for the morphology of the T wave in unipolar electrograms,” *Am. J. Physiol.-Heart Circ. Physiol.*, vol. 297, no. 2, pp. H792–H801, 2009.
[96] D. Western, B. Hanson, and P. Taggart, “Measurement bias in activation-recovery intervals from unipolar electrograms,” *Am. J. Physiol.-Heart Circ. Physiol.*, vol. 308, no. 4, pp. H331–H338, 2015.
[97] M. P. Nash, C. P. Bradley, and D. J. Paterson, “Imaging electrocardiographic dispersion of depolarization and repolarization during ischemia,” *Circulation*, vol. 107, no. 17, pp. 2257–2263, 2003.
[98] Y. Liang *et al.*, “QT dispersion failed to estimate the global dispersion of ventricular repolarization measured using monophasic action potential mapping technique in swine and patients,” *J. Electrocardiol.*, vol. 38, no. 1, pp. 19–27, 2005.
[99] J. E. Burnes, R. N. Ghanem, A. L. Waldo, and Y. Rudy, “Imaging dispersion of myocardial repolarization, I,” *Circulation*, vol. 104, no. 11, pp. 1299–1305, 2001.
[100] C. Ramanathan, R. N. Ghanem, P. Jia, K. Ryu, and Y. Rudy, “Noninvasive electrocardiographic imaging for cardiac electrophysiology and arrhythmia,” *Nat. Med.*, vol. 10, no. 4, pp. 422–428, 2004.
[101] M. J. Burgess, “Relation of ventricular repolarization to electrocardiographic T wave-form and arrhythmia vulnerability,” *Am. J. Physiol.-Heart Circ. Physiol.*, vol. 236, no. 3, pp. H391–H402, 1979.
[102] C. Han, S. M. Pogwizd, C. R. Killingsworth, and B. He, “Noninvasive imaging of three-dimensional cardiac activation sequence during pacing and ventricular tachycardia,” *Heart Rhythm*, vol. 8, no. 8, pp. 1266–1272, 2011.
[103] M. S. Spach and R. C. Barr, “Anaylsis of ventricular activation and repolarization from intramural and epicardial potential distributions for ectopic beats in the intact dog.,” *Circ. Res.*, vol. 37, no. 6, pp. 830–843, 1975.
[104] C. Ramanathan, P. Jia, R. Ghanem, K. Ryu, and Y. Rudy, “Activation and repolarization of the normal human heart under complete physiological conditions,” *Proc. Natl. Acad. Sci.*, vol. 103, no. 16, pp. 6309–6314, 2006.
[105] B. Hanson *et al.*, “Interaction of Activation–Repolarization Coupling and Restitution Properties in HumansCLINICAL PERSPECTIVE,” *Circ. Arrhythm. Electrophysiol.*, vol. 2, no. 2, pp. 162–170, 2009.
[106] A. M. Yue, T. R. Betts, P. R. Roberts, and J. M. Morgan, “Global dynamic coupling of activation and repolarization in the human ventricle,” *Circulation*, vol. 112, no. 17, pp. 2592–2601, 2005.
[107] E. Corday, V. Bazika, T.-W. Lang, S. Pappelbaum, H. Gold, and H. Bernstein, “Detection of Phantom Arrhythmias and Evanescent Electrocardiographic Abnormalities: Use of Prolonged Direct Electrocardiocording,” *JAMA*, vol. 193, no. 6, pp. 417–421, Aug. 1965.

[108] M. E. Josephson, H. L. Waxman, M. E. Cain, M. J. Gardner, and A. E. Buxton, “Ventricular activation during ventricular endocardial pacing. II. Role of pace-mapping to localize origin of ventricular tachycardia,” *Am. J. Cardiol.*, vol. 50, no. 1, pp. 11–22, Jul. 1982.
[109] R. L. Jadonath, D. S. Schwartzman, M. W. Preminger, C. D. Gottlieb, and F. E. Marchlinski, “Utility of the 12-lead electrocardiogram in localizing the origin of right ventricular outflow tract tachycardia,” *Am. Heart J.*, vol. 130, no. 5, pp. 1107–1113, 1995.
[110] S. Kamakura *et al.*, “Localization of optimal ablation site of idiopathic ventricular tachycardia from right and left ventricular outflow tract by body surface ECG,” *Circulation*, vol. 98, no. 15, pp. 1525–1533, 1998.
[111] M. E. Josephson and D. J. Callans, “Using the twelve-lead electrocardiogram to localize the site of origin of ventricular tachycardia,” *Heart Rhythm*, vol. 2, no. 4, pp. 443–446, 2005.
[112] R. Setiono and H. Liu, “Neural-network feature selector,” *IEEE Trans. Neural Netw.*, vol. 8, no. 3, pp. 654–662, May 1997.
[113] H. A. Rowley, S. Baluja, and T. Kanade, “Neural network-based face detection,” *IEEE Trans. Pattern Anal. Mach. Intell.*, vol. 20, no. 1, pp. 23–38, Jan. 1998.
[114] P. D. Heermann and N. Khazenie, “Classification of multispectral remote sensing data using a back-propagation neural network,” *IEEE Trans. Geosci. Remote Sens.*, vol. 30, no. 1, pp. 81–88, Jan. 1992.
[115] G. M. Foody and M. K. Arora, “An evaluation of some factors affecting the accuracy of classification by an artificial neural network,” *Int. J. Remote Sens.*, vol. 18, no. 4, pp. 799–810, Mar. 1997.
[116] H.-S. Chow, G. B. Moody, and R. G. Mark, “Detection of ventricular ectopic beats using neural networks,” in *Computers in Cardiology 1992, Proceedings of*, 1992, pp. 659–662.
[117] P. de Chazal and R. B. Reilly, “Automatic classification of ECG beats using waveform shape and heart beat interval features,” in *Acoustics, Speech, and Signal Processing, 2003. Proceedings.(ICASSP’03). 2003 IEEE International Conference on*, 2003, vol. 2, p. II–269.
[118] S. Osowski and T. H. Linh, “ECG beat recognition using fuzzy hybrid neural network,” *IEEE Trans. Biomed. Eng.*, vol. 48, no. 11, pp. 1265–1271, 2001.
[119] H. Gothwal, S. Kedawat, R. Kumar, and others, “Cardiac arrhythmias detection in an ECG beat signal using fast fourier transform and artificial neural network,” *J. Biomed. Sci. Eng.*, vol. 4, no. 04, p. 289, 2011.
[120] K. Minami, H. Nakajima, and T. Toyoshima, “Real-time discrimination of ventricular tachyarrhythmia with Fourier-transform neural network,” *IEEE Trans. Biomed. Eng.*, vol. 46, no. 2, pp. 179–185, 1999.
[121] Y. Kaya and H. Pehlivan, “Classification of Premature Ventricular Contraction in ECG,” *Int J Adv Comput Sci Appl*, vol. 6, no. 7, pp. 34–40, 2015.
[122] N. Allahverdi, G. Altan, and Y. Kutlu, “Diagnosis of Coronary Artery Disease Using Deep Belief Networks,” in *2. Int. Conf. Eng. Nat. Sci*, p. 9.
[123] Y. Özbay, R. Ceylan, and B. Karlik, “A fuzzy clustering neural network architecture for classification of ECG arrhythmias,” *Comput. Biol. Med.*, vol. 36, no. 4, pp. 376–388, 2006.
[124] M. Javadi, R. Ebrahimpour, A. Sajedin, S. Faridi, and S. Zakernejad, “Improving ECG classification accuracy using an ensemble of neural network modules,” *PLoS One*, vol. 6, no. 10, p. e24386, 2011.
[125] S. Kiranyaz, T. Ince, and M. Gabbouj, “Real-Time Patient-Specific ECG Classification by 1-D Convolutional Neural Networks,” *IEEE Trans. Biomed. Eng.*, vol. 63, no. 3, pp. 664–675, Mar. 2016.
[126] B. Hedén, H. Öhlin, R. Rittner, and L. Edenbrandt, “Acute myocardial infarction detected in the 12-lead ECG by artificial neural networks,” *Circulation*, vol. 96, no. 6, pp. 1798–1802, 1997.

[127] T. Stamkopoulos, K. Diamantaras, N. Maglaveras, and M. Strintzis, "ECG analysis using nonlinear PCA neural networks for ischemia detection," *IEEE Trans. Signal Process.*, vol. 46, no. 11, pp. 3058–3067, 1998.
[128] H. Haraldsson, L. Edenbrandt, and M. Ohlsson, "Detecting acute myocardial infarction in the 12-lead ECG using Hermite expansions and neural networks," *Artif. Intell. Med.*, vol. 32, no. 2, pp. 127–136, 2004.
[129] M. D. Cerqueira *et al.*, "Standardized myocardial segmentation and nomenclature for tomographic imaging of the heart. A statement for healthcare professionals from the Cardiac Imaging Committee of the Council on Clinical Cardiology of the American Heart Association," *Circulation*, vol. 105, no. 4, pp. 539–542, Jan. 2002.
[130] F. Sacher *et al.*, "Epicardial ventricular tachycardia ablation," *J. Am. Coll. Cardiol.*, vol. 55, no. 21, pp. 2366–2372, 2010.
[131] P. Della Bella *et al.*, "Epicardial Ablation for Ventricular TachycardiaClinical Perspective," *Circ. Arrhythm. Electrophysiol.*, vol. 4, no. 5, pp. 653–659, 2011.
[132] J. Fernández-Armenta and A. Berruezo, "How to recognize epicardial origin of ventricular tachycardias?," *Curr. Cardiol. Rev.*, vol. 10, no. 3, pp. 246–256, 2014.
[133] A. Berruezo, L. Mont, S. Nava, E. Chueca, E. Bartholomay, and J. Brugada, "Electrocardiographic recognition of the epicardial origin of ventricular tachycardias," *Circulation*, vol. 109, no. 15, pp. 1842–1847, 2004.
[134] P. M. van Dam, T. F. Oostendorp, and A. van Oosterom, "Application of the fastest route algorithm in the interactive simulation of the effect of local ischemia on the ECG," *Med. Biol. Eng. Comput.*, vol. 47, no. 1, pp. 11–20, Jan. 2009.
[135] P. M. van Dam, R. Tung, K. Shivkumar, and M. Laks, "Quantitative localization of premature ventricular contractions using myocardial activation ECGI from the standard 12-lead electrocardiogram," *J. Electrocardiol.*, vol. 46, no. 6, pp. 574–579, 2013.
[136] D. Potyagaylo, O. Dössel, and P. van Dam, "Influence of Modeling Errors on the Initial Estimate for Nonlinear Myocardial Activation Times Imaging Calculated With Fastest Route Algorithm," *IEEE Trans. Biomed. Eng.*, vol. 63, no. 12, pp. 2576–2584, Dec. 2016.
[137] R. Cabrera-Lozoya, B. Berte, H. Cochet, P. Jaïs, N. Ayache, and M. Sermesant, "Image-Based Biophysical Simulation of Intracardiac Abnormal Ventricular Electrograms," *IEEE Trans. Biomed. Eng.*, vol. 64, no. 7, pp. 1446–1454, Jul. 2017.
[138] T. Yang, L. Yu, Q. Jin, L. Wu, and B. He, "Localization of Origins of Premature Ventricular Contraction by Means of Convolutional Neural Network from 12-lead ECG," *IEEE Trans. Biomed. Eng.*, vol. PP, no. 99, pp. 1–1, 2017. © [2017] IEEE. Reprinted, with permission, from [Ting Yang, Localization of Origins of Premature Ventricular Contraction by Means of Convolutional Neural Network from 12-lead ECG, IEEE Transactions on Biomedical Engineering, and 09/2017]
[139] "Deep Learning Toolbox - File Exchange - MATLAB Central." [Online]. Available: http://www.mathworks.com/matlabcentral/fileexchange/38310-deep-learning-toolbox. [Accessed: 11-Aug-2017].
[140] S. Giffard-Roisin *et al.*, "Non-Invasive Personalisation of a Cardiac Electrophysiology Model from Body Surface Potential Mapping," *IEEE Trans. Biomed. Eng.*, vol. PP, no. 99, pp. 1–1, 2017.

Appendix Publication List

Journal Papers

Yang T, Yu L, Jin Q, Wu L, He B. Localization of Origins of Premature Ventricular Contraction by Means of Convolutional Neural Network from 12-lead ECG. *IEEE Trans. Biomed. Eng.*, vol. PP, no. 99, pp. 1–1, 2017.

Yang T, Yu L, Jin Q, Wu L, He B. Activation Recovery Interval Imaging of Premature Ventricular Contraction (submitted)

Yang T, Yu L, Walcott G.P, Pogwizd S.M, He B. Noninvasive Activation Imaging of Ventricular Arrhythmias by Spatial Gradient Sparse in Frequency Domain: Application to Reentrant Ventricular Tachycardia in a Late Myocardial Infarction Swine Model (submitted)

Zhou Z, Han C, **Yang T**, He B. Noninvasive Imaging of 3-Dimensional Myocardial Infarction From the Inverse Solution of Equivalent Current Density in Pathological Hearts. *IEEE Trans. Biomed. Eng.*, vol. 62, no. 2, pp. 468–476, Feb. 2015.

Conference Abstracts

Yang T, Zhou Z, He B. Finite Element Modeling of Myocardial Infarction, Institute for Engineering in Medicine: The Annual Conference and Retreat, Session of Cardiovascular Engineering, 2014.

Yang T, Yu L, He B. An Entropy-based Noninvasive Cardiac Imaging of Atrial Fibrillation, The Design of Medical Devices Conference, 2015.

Yang T, Yu L, Walcott G.P, He B, Pogwizd S.M. 3D Intracardiac Mapping of Reentrant Tachycardia in a Swine Model with Myocardial Infarction, Institute for Engineering in Medicine: The Annual Conference and Retreat, Session of Medical and Biological Imaging, 2015.

Yu L, Pogwizd S, McElderry HT, **Yang T**, He B. Non-invasive Three Dimensional Imaging of Ventricular Arrhythmias: In-procedure Simultaneous Mapping of Ventricular

Tachycardia and Premature Ventricular Complexes. Circulation. 2015 Nov 10; 132(Suppl 3):A18237-A18237. American Heart Association Scientific Sessions 2015.

Yang T, Yu L, Jin Q, Wu L, He B. Activation Recovery Interval Imaging for Premature Ventricular Contraction Patients – A Pilot Study. International Conference of the IEEE Engineering in Medicine and Biology Society, Cardiovascular & Respiratory Systems Engineering, 2016. (2-minute Oral Presentation)

Yu L, Pogwizd S.M, Walcott G.P, **Yang T**, He B. Three Dimensional Non-Invasive Imaging of Reentrant VT in Swine with Myocardial Infarction. Circulation. 2016; 134: A19036. American Heart Association Scientific Sessions 2016.

Yang T, Yu L, He B. Localization of Premature Ventricular Contractions Using Convolutional Neural Network from 12-lead Electrocardiogram. American Heart Association Scientific Sessions 2017.